Characteristic Slow-Slip Events on the Superstition Hills Fault, Southern California

Ellis Vavra[1], Yuri Fialko[2], Thomas K. Rockwell[3], Roger Bilham[4], Petra Stepancikova[5], Jakub Stemberk[6], Petr Táboří k[7], and Josef Stemberk[8]

[1]Scripps Institution of Oceanography
[2]UCSD
[3]San Diego State University
[4]CIRES, Univ Colorado, Department of Geological Sciences
[5]Institute of Rock Structure and Mechanics, Academy of Sciences of the Czech Republic
[6]Institute of Rock Structure and Mechanics of the Czech Academy of Sciences
[7]Charles University, Faculty of Science, Institute of Hydrogeology, Engineering Geology and Applied Geophysics
[8]Department of Engineering Geology, Institute of Rock Structure & Mechanics, v.v.i.

December 10, 2023

Abstract

The Superstition Hills Fault (SHF) exhibits a rich spectrum of slip modes, including M 6+ earthquakes, afterslip, quasi-steady creep, and both triggered and spontaneous slow slip events (SSEs). Following 13 years of quiescence, creepmeters recorded 25 mm of slip during 16-19 May 2023. Additional sub-events brought the total slip to 41 mm. The event nucleated on the northern SHF in early-May and propagated bi-laterally at rates on the order of kilometers per day. Surface offsets reveal a bi-modal slip distribution, with slip on the northern section of the fault being less localized and lower amplitude compared to the southern section. Kinematic slip models confirm systematic variations in the slip distribution along-strike and with depth and suggest that slip is largely confined to the shallow sedimentary layer. Observations and models of the 2023 SSE bear a strong similarity to previous slip episodes in 1999, 2006, and 2010, suggesting a characteristic behavior.

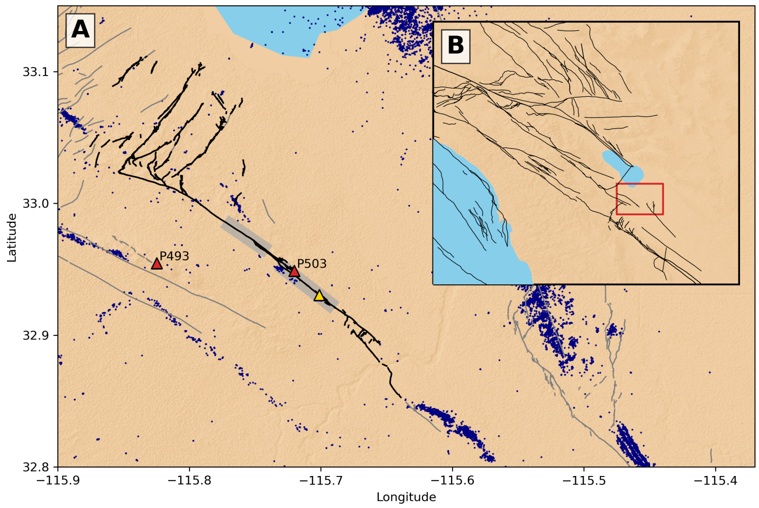
A
B
P493
P503
Latitude
Longitude
33.1
33.0
32.9
32.8
−115.9
−115.8
−115.7
−115.6
−115.5
−115.4

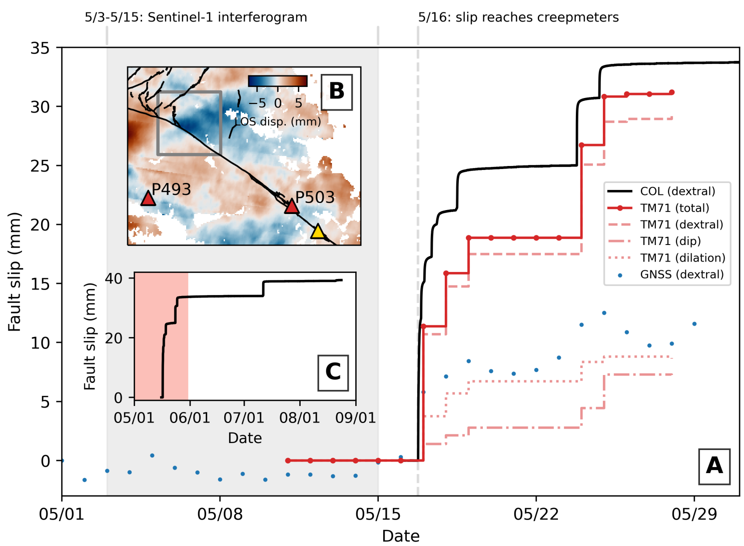
5/3-5/15: Sentinel-1 interferogram
5/16: slip reaches creepmeters
A
B
C
LOS disp. (mm)
P493
P503
Fault slip (mm)
Date
COL (dextral)
TM71 (total)
TM71 (dextral)
TM71 (dip)
TM71 (dilation)
GNSS (dextral)
05/01
05/08
05/15
05/22
05/29
06/01
07/01
08/01
09/01

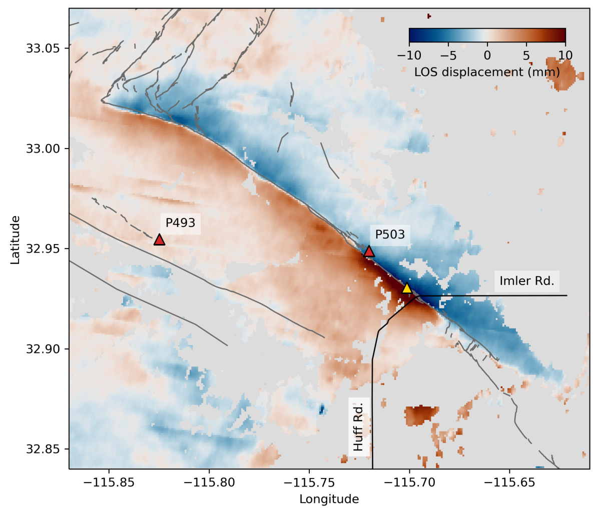
−10 −5 0 5 10
LOS displacement (mm)
P493
P503
Imler Rd.
Huff Rd.
Latitude
33.05
33.00
32.95
32.90
32.85
−115.85 −115.80 −115.75 −115.70 −115.65
Longitude

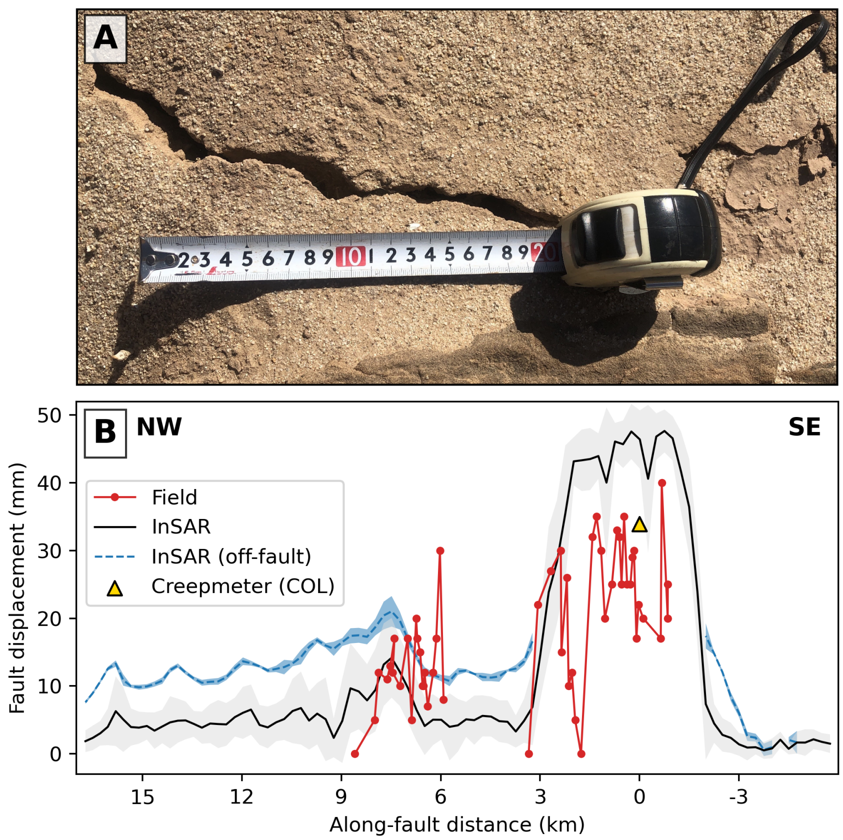
A
2 3 4 5 6 7 8 9 10 1 2 3 4 5 6 7 8 9 20
B
NW
SE
Field
InSAR
InSAR (off-fault)
Creepmeter (COL)
Fault displacement (mm)
50
40
30
20
10
0
15 12 9 6 3 0 -3
Along-fault distance (km)

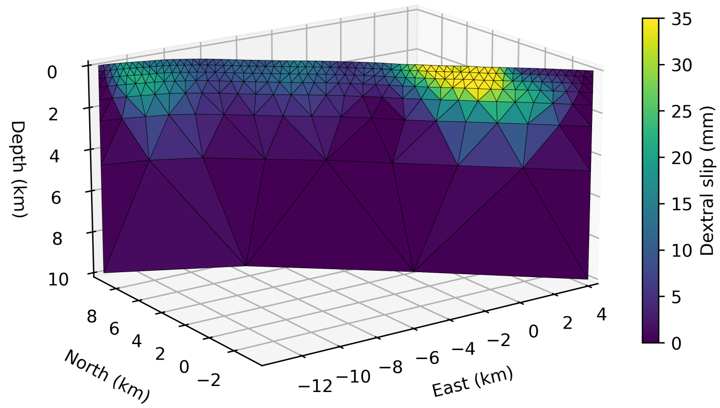
Depth (km)
0
2
4
6
8
10
North (km)
8
6
4
2
0
−2
East (km)
−12
−10
−8
−6
−4
−2
0
2
4
Dextral slip (mm)
35
30
25
20
15
10
5
0

Characteristic Slow-Slip Events on the Superstition Hills Fault, Southern California

Ellis J. Vavra[1], Yuri Fialko[1], Thomas Rockwell[2], Roger Bilham[3], Petra Štěpančíková[4], Jakub Stemberk[4], Petr Tábořík[4], Josef Stemberk[4]

[1]Institute of Geophysics and Planetary Physics, Scripps Institution of Oceanography, University of California, San Diego, La Jolla, CA, USA
[2]Department of Geological Sciences, San Diego State University, San Diego, CA, USA
[3]Cooperative Institute for Research in Environmental Sciences, University of Colorado, Boulder, CO, USA
[4]Institute of Rock Structure and Mechanics, Czech Academy of Sciences, Prague, Czech Republic

Key Points:

- We document a recent spontaneous slow slip event on the Superstition Hills Fault using creepmeter, InSAR, GNSS, and field measurements.
- Over 41 mm of slip occurred from mid-May to mid-July 2023, with moment release corresponding to a M_w 5.0 earthquake.
- The kinematics of the 2023 event are remarkably similar to several previous slow slip events, suggesting a characteristic rupture process.

Corresponding author: Ellis J. Vavra, evavra@ucsd.edu

Abstract

The Superstition Hills Fault (SHF) exhibits a rich spectrum of slip modes, including M 6+ earthquakes, afterslip, quasi-steady creep, and both triggered and spontaneous slow slip events (SSEs). Following 13 years of quiescence, creepmeters recorded 25 mm of slip during 16-19 May 2023. Additional sub-events brought the total slip to 41 mm. The event nucleated on the northern SHF in early-May and propagated bi-laterally at rates on the order of kilometers per day. Surface offsets reveal a bi-modal slip distribution, with slip on the northern section of the fault being less localized and lower amplitude compared to the southern section. Kinematic slip models confirm systematic variations in the slip distribution along-strike and with depth and suggest that slip is largely confined to the shallow sedimentary layer. Observations and models of the 2023 SSE bear a strong similarity to previous slip episodes in 1999, 2006, and 2010, suggesting a characteristic behavior.

Plain Language Summary

Studying the mechanical properties and behavior of faults is essential for understanding earthquake ruptures. In this study, we investigate a recent slip event on the Superstition Hills Fault (SHF), which has a well-documented record of slip. A notable aspect of the SHF is that it periodically undergoes "slow slip events" (SSEs), where the fault slips and releases energy without any accompanied ground shaking. During May-July 2023, the SHF experienced a major SSE for the first time in 13 years. Our analysis shows that it was the largest documented SSE on the SHF and released equivalent energy to a magnitude 5 earthquake. We also find that the spatial pattern of fault slip is very similar to several previous slip events in 1999, 2006, and 2010, suggesting that the SHF has a tendency to slip in a characteristic manner.

1 Introduction

The Superstition Hills Fault (SHF) is located at the southern end of the San Jacinto Fault Zone (SJFZ), 35 km north of the United States-Mexico border in Southern California (e.g., Sharp, 1967; Hudnut & Sieh, 1989; Tymofyeyeva & Fialko, 2018). The SHF has a well-documented record of time-dependent slip, spanning the coseismic, postseismic, and interseismic phases of the earthquake cycle. Early observations dating back to 1960s detected surface creep along the SHF at an average rate of 0.5 mm/yr (Louie et al., 1985), as well as episodes of accelerated slip triggered by local earthquakes (Allen et al., 1972; Fuis, 1982; Sharp et al., 1986).

On 24 Nov 1987, the SHF ruptured in a M_S 6.6 earthquake with 1 m of average coseismic slip below 5 km depth (Wald et al., 1990). Significant surface slip was delayed by minutes or hours, but within a day was quantified as rapidly developing afterslip (Sharp et al., 1986; Williams & Magistrale, 1989), that in the following 3 years decayed to low rates, cumulatively matching coseismic slip at depth (Bilham et al., 2016). The rate of decay of afterslip was interpreted in terms of velocity-strengthening behavior of the uppermost 5 km of the fault (Marone et al., 1991; Barbot et al., 2009). Several years later, the 1992 M_w 7.3 Landers and M_w 6.2 Big Bear earthquakes triggered 8+ mm of slip at the site of a creepmeter operated by CU Boulder, and up to 20 mm elsewhere (Bodin et al., 1994; Rymer, 2000). The 1999 M_w 7.1 Hector Mine earthquake triggered surface slip of up to 18 mm along at least 9 km of the SHF (Rymer et al., 2002).

Most of the observed shallow creep events on the SHF appear to be dynamically triggered by regional (e.g. Allen et al., 1972; Louie et al., 1985; Hauksson et al., 2013; Wei et al., 2011) or teleseismic (Heflin et al., 2020) earthquakes. This is similar to the behavior observed on other major faults in the area that exhibit shallow creep, in particular the Southern San Andreas Fault (e.g., Bodin et al., 1994; Fialko, 2006; Tymofyeyeva et al., 2019). However, some shallow creep events on the SHF occur spontaneously (Wei et al., 2009), analogous to Slow Slip Events (SSE) observed on megathrusts in subduction zones (e.g., Dragert et al., 2001; LaBonte et al., 2009; Wallace, 2020).

The first reported spontaneous SSE on the SHF occurred in 2006 and produced $\sim$30 mm of surface slip over a time period of two weeks, with most of the slip occurring in the first three days (Wei et al., 2009). Inversions of the ENVISAT Interferometric Synthetic Aperture Radar (InSAR) data capturing the 2006 event showed that the latter was equivalent to a M_w 4.7 earthquake and that slip was largely confined to shallowest 2-3 km of the crust, consistent with the inferred depth of sediments (Kohler & Fuis, 1986; Williams & Magistrale, 1989; Wei et al., 2009). A comparable-size SSE with a similar slip pattern was triggered by the 2010 M_w 7.2 El Mayor-Cucapah earthquake (Wei et al., 2011; Donnellan et al., 2014). Wei et al. (2015) examined ERS-1/2 InSAR data spanning 1992-2004 (during which no creepmeter measurements were made), and detected at least four more events. The first and second events occurred between November 1993-

July 1995, and October-December 1996, respectively, and each produced about 20 mm of slip. The third and fourth events occurred in 1997 and 1998, respectively, but were limited to the northern half of the fault. Additional minor slip on the SHF was triggered by a pair of M_w 5+ earthquakes in the 2012 Brawley Swarm, as well as the teleseismic 2017 M_w 8.2 Chiapas (Mexico) earthquake (Hauksson et al., 2013; Heflin et al., 2020).

In this study, we present observations and models of a new spontaneous SSE which began in May 2023. We show that the latest SSE is the largest observed shallow slip event yet recorded on the SHF, and that it bears a strong resemblance to previous events (in particular, the spontaneous 2006, as well as the triggered 1999 and 2010 events), suggesting a characteristic rupture pattern.

2 Data and Methods

The 2023 SSE was initially detected by two creepmeters installed on the southern SHF, 700 m northwest of Imler Road (Figure 3). The Colorado (COL) creepmeter records slip at 1-minute intervals and consists of a 6-m-long, 4-mm-diameter pultruded carbon rod anchored ±1.5 m from the fault trace (Bilham & Castillo, 2020). The TM71 creepmeter consists of two Moiré-fringe optical sensors arranged to measure strike-slip, dip-slip, and dilation, from which the total displacement vector can be calculated (Košťák, 1969; Klimeš et al., 2012; Martí et al., 2013). TM71 samples at daily intervals and is anchored ±0.5 m on either side of the fault trace. Both instruments recorded an abrupt onset of a slip event on 16 May 2023 (Figure 2A). Additional details on the creepmeters are provided in the Supporting Information.

Similar, albeit smaller-amplitude, slip was registered by continuously-operating Global Navigation Satellite System (GNSS) station P503, located ∼3 km northwest of the creepmeters and ∼300 m east from the fault trace (Figure 1). To remove noise due to common-mode regional signals, we computed the change in fault-parallel baseline between station P503 and station P493 (Figures 1 & 2).

The 2023 SSE was also imaged by the European Space Agency's Sentinel-1A synthetic aperture radar satellite. We used data from Sentinel-1A's descending track 173 to map surface deformation associated with the slip episode. Unfortunately, no acquisitions were made from the ascending track covering the area of interest. We used the acquisition from 3 May 2023 as reference and processed interferograms using all data collected between October 2022-November 2023. To suppress atmospheric contributions, which are the dominant source of noise for measuring small-amplitude deformation (e.g., Zebker et al., 1997; Pearse & Fialko, 2010; Nof et al., 2012), we used a Common Scene Stacking method (Tymofyeyeva & Fialko, 2015) to estimate atmospheric phase screens (APS) for 3 May and 26 July acquisitions. To do so, we generated all interferometric pairs with the 3 May end date, and the 26 July start date. We chose pairs that minimize the perpendicular baseline, and are least affected by decorrelation. The resulting subsets were averaged to obtain APS for the respective common scenes. We inspected the estimated APS to ensure that no fault slip occurred outside of the 3 May - 26 July 2023 interval, which might bias our deformation measurements, and subtracted the estimated APS from the 3 May - 26 July interferogram (Figure 3). For interferograms that span shorter time periods during the SSE, we only applied the correction for the start date (3-15 May, Figures 2B, S1, & S2; 3 May-8 June, Figures 4 & S3).

To evaluate slip along the fault trace, we computed offsets from fault-perpendicular swaths at 250 m intervals along the fault. We also computed the maximum observed surface offsets for cases where slip is distributed across a shear zone of finite width, as opposed to localized on the fault trace (Figures S2 & S3). Further details on the offset estimation procedures can be found in the Supporting Information. Figure 4B shows the along-fault distribution of surface slip measured by InSAR.

We also conducted field surveys to document surface expressions of shallow creep, verify the rupture extent, and measure offsets for comparisons with other datasets. Preliminary field investigations on 20 May 2023 revealed evidence of cracking and centimeter-scale offsets along the fault trace near Imler Road and the creepmeters. A more detailed survey on 11 June 2023 mapped surface cracks and measured their offsets (Figures 4A & S4) along much of the SHF. The southern section of the SHF produced a localized surface rupture that could be easily traced for several kilometers both north and south of the creepmeters (Figures 1A & 4B). Further to the north, surface expressions of shallow creep become less obvious, likely due to a distributed nature of surface deformation (Figure S3) and possibly an increased presence of loose sand. Overall, the measured offsets on the northern SHF are smaller than those on the southern SHF (Figure 4B). A $\sim$3 km stretch north of the fault step-over near the GNSS site P503 (Figure 1A) was not mapped due to logistical constraints.

3 Evolution of Fault Slip During the 2023 SSE

High-rate data from the COL creepmeter recorded the onset of the 2023 slip event on 16 May at 18:29 UTC (11:29 PDT, local time) at the location of the creepmeter (see Figure 2A). Retroactive analysis of 12-day Sentinel-1A interferograms reveals that the SSE likely nucleated sometime between 3-15 May 2023 on the northern SHF (Figures 2B, S1, & S2) and propagated to the south. Investigation of both regional and global seismic catalogs does not reveal potential triggers (see Supporting Information for details), suggesting slip initiated spontaneously. The southernmost extent of slip that occurred between 3-15 May 2023 was approximately ∼10 km from the creepmeters (Figure S1), implying an along-strike rupture velocity on the order of kilometers per day.

Over 20 mm of slip occurred within 24 hours after the slip front reached the creepmeters, and over 80% of slip registered by the creepmeters occurred in first two weeks of the event (Figure 2A & 2C). A 5 mm sub-event on 11 July 2023 brought the total amplitude of the SSE to 41 mm near Imler Road (Figure 2C). InSAR data indicate that slip propagated both northwest and southeast along-strike (Figures S2 & S3), rupturing the entire shallow section of the SHF. The main slip patch is observed within several km of the creepmeters on the southern segment of the SHF, with ∼45 mm of slip accumulating by mid-June 2023 (Figure 4B). Slip on the northern segment (3-15 km northwest of the creepmeters) was on average ∼5 mm, with a small peak 7-8 km north of the creepmeters (Figure 4). However, the InSAR data show that slip on the northern section was distributed across a shear zone 400-1300 m wide (Figure S3), so that the maximum fault-parallel displacements occurred away from the fault trace, amounting to 10-20 mm (Figure 4B).

Figure 4B shows a comparison of surface offsets along the SHF measured using different techniques. While the data in general show good agreement, some systematic differences are apparent. In particular, the InSAR-derived offsets are larger compared to the field and creepmeter measurements (the only exception is a ∼30 mm offset suggested by field observations at ∼6 km northwest from the creepmeters, see Figure 4B; this data point may be biased due to erosion of surface cracks in soft sediments). Such differences are expected if fault creep is not perfectly localized on a fault trace. All three observations are collocated near Imler Road and the measured slip increases with the observation aperture (centimeters for field measurements, meters for creepmeters, and hundreds of meters for InSAR).

InSAR data also indicate that slip on the southern section of the SHF occurs in a zone narrower than $\sim$100 m (Figure S3), much more localized compared to slip on the northern section. It was suggested that continuous across-fault variations in surface displacements due to fault slip might result from a strong shallow layer resisting the propagation of slip to the Earth's surface, resulting in a "surface locking depth" (Brooks et al., 2017; Parker et al., 2021). However, given the low mechanical strength of near-surface sediments, a more plausible explanation is that the effective width of the shear zone reflects distributed failure within the fault damage zone with depth comparable to (or greater than) its width (Fialko et al., 2002; Lindsey, Fialko, et al., 2014). Comparisons of surface ruptures from InSAR and field surveys for the 2006 and 2010 SSEs reveal a similar pattern (Wei et al., 2009, 2011), suggesting that some fraction of shallow creep may be accommodated by off-fault deformation (Fialko et al., 2005; Jin et al., 2022).

To evaluate the subsurface distribution of slip on the SHF due to the 2023 SSE, we performed kinematic inversions of the InSAR line-of-sight displacements (Figure 3) using an elastic halfspace dislocation model (see the Supporting Information for details). Our preferred slip model is shown in Figure 5 and features two primary asperities corresponding to the northern and southern sections of the SHF. Slip on the southern section is higher amplitude (>30 mm) and maximum at the surface, while slip on the northern section is more subdued (<20 mm) and has a maximum at depth of 1-2 km. The apparent "shallow slip deficit" (SSD) on the northern section of the SHF is likely an artifact of a distributed failure (Figure S3) that is not accounted for by our purely elastic model (Barbot et al., 2008; Lindsey, Sahakian, et al., 2014). The gap between the two slip patches corresponds to the step-over between the northern and southern SHF segments (Figures 1 & 3). Overall, slip is limited to the depth of sedimentary cover in the Imperial Valley (<4 km; Kohler & Fuis, 1986; Wei et al., 2009; Lindsey & Fialko, 2016). Converting the total slip from our preferred model (Figure 5) to moment magnitude, using shear modulus of 33 GPa, we estimate that the 2023 SSE is equivalent to a M_w 5.0 earthquake, making it the largest documented SSE on the SHF to date.

4 Discussion

The growing catalog of aseismic slip events on the SHF enables a comparative analysis of the observed slip distributions. Each of the well-observed 2006, 2010, and 2023 SSEs is characterized by higher slip on the southern segment of the SHF, and lower slip on the northern segment (Figure 5). This spatial pattern was likely similar for the 1999 Hector Mine triggered slip, although the northern SHF was not mapped in-detail (perhaps due to the difficulty in finding surface offsets in zones of distributed shear; Rymer et al., 2002). The respective ratios of slip amplitudes at the southern and northern fault sections are about 2:1 (Figure 3). Given that the entire fault appears to have slipped in the top few km of the crust during the 2006, 2010, and 2023 SSEs (Figure 5; Wei et al., 2009, 2011), the largest SSEs occur as "characteristic" ruptures, with more strain release on the southern section of the SHF. This raises a question about the resulting "strain surplus" on the northern SHF.

One possibility is that the systematic along-strike variations in surface slip (Figure 3) result from variations in the sediment thickness (Wei et al., 2009). Assuming that shallow creep is limited to the sedimentary layer, the magnitude of surface slip is expected to scale with the sediment depth (e.g., Kaneko et al., 2013). In this case, lower slip during the interseismic period should be compensated by higher coseismic slip. However, the observed surface slip due to the 1989 Superstition Hills earthquake was essentially the same on the northern and southern sections of the SHF (Sharp et al., 1989). Another possibility is that the observed smaller slip on the northern SHF during "system-size" SSEs (Figures 3 & 5) is compensated by smaller SSEs that rupture only the northern SHF. There is some evidence for such events from the InSAR observations (Wei et al., 2015). The available data may not be sufficient to determine the average slip balance during the interseismic period, but it is clear that shallow creep on the SHF exhibits substantial spatio-temporal complexity, with both fault-wide and partial ruptures in the uppermost crust, heterogeneous slip distributions, variable near-surface slip localization, and rapid variations in slip rate (Figure 2). Moreover, unlike the two most recent spontaneous creep events (2006 and 2023) that were associated with slip durations of weeks, slip triggered by the El Major-Cucapah earthquake in 2010 was complete between two five-minute samples of the creepmeter. These features are not predicted by classic models of rate-state faults with the velocity-strengthening shallow layer (e.g., Li & Rice, 1987; Kaneko et al., 2013).

The interval between episodic creep events following the 1987 earthquake has steadily increased from months to several years. These intervals are apparently shortened by the premature release of an accumulating SSD by shaking during major nearby earthquakes. For example, it is probable that the atypically abrupt surface slip induced by the 2010 El Major-Cucapah earthquake efficiently released a SSD that would otherwise have been accumulated and released within several years as a spontaneous creep event. The transition from rapid afterslip process to an episodic creep appears to have occurred starting 1995$\pm$3 years, since when 15 cm of slip has been released in six creep events. Afterslip presumably continues to contribute to surface slip because the intervals between episodic events increases during these 28 years (i.e. shallow slip is not yet entirely attributable to the release of antiplane shear strain arising from interseismic deformation).

From 2004-May 2023, the averaged creep rate was 3.2 mm/yr ($\sim$5 mm/yr if including the 2023 event). The rate would be 3.2 mm/yr if we suppose that no spontaneous creep event occurs for a further decade, and 4.7 mm/yr should a $\sim$40 mm event occur after this interval. These estimates are lower than the maximum long term geological slip rate of 6 mm/yr adopted by Field et al. (2015), based largely on a 660 year geological slip rate of 2-6 mm/yr determined by Hudnut and Sieh (1989). However, the average shallow creep rate should be a small fraction of the geologic slip rate, depending on the locking depths at the top and bottom of the seismogenic layer (e.g., Lindsey & Fialko, 2016). This implies a geologic slip rate on the SHF in excess of 10 mm/yr, higher than that assumed in the Uniform California Earthquake Rupture Forecast v.3 (UCERF3; Field et al., 2014), but consistent with the suggestion that the SHF is a continuation of the main strand of the San Jacinto fault with a slip rate of $\sim$15 mm/yr (Tymofyeyeva & Fialko, 2018; Vavra et al., 2023).

5 Conclusions

We document the occurrence of a slow slip event (SSE) on the Superstition Hills Fault (SHF) which began in May 2023 and incremented in $\leq$5 mm slip events, at uneven but increasing intervals for the following 60 days. InSAR measurements indicate the SSE likely initiated near the northern end of the fault and propagated $\sim$15 km to the south over the course of several days. Creepmeters on the southern SHF recorded up to 25 mm of dextral slip over the course of 3 days, with slip eventually attaining 41 mm by mid-July 2023. Fault offsets computed from InSAR data suggest maximum surface slip of 45+ mm. While slip is highly localized along a region of high slip on the southern end of the rupture, surface deformation along the northern ∼12 km of the fault is characterized by distributed shear over 400-1300 m. Finite fault models derived from InSAR data indicate that the fault slip during the SSE was largest on the southern SHF. On the northern SHF, the average slip amplitude was lower by about a factor of two. Finite fault models also show that slip is largely confined to the shallowest 4 km of the fault, consistent with the depth of sediments and results inferred from previous SHF events. The moment release throughout the entire SSE sequence was equivalent to a $M_w \sim 5.0$ earthquake. The similarity of the 2023 SSE to previous events dating back to at least 2006 suggests spontaneous SSEs on the SHF have ruptured largely the same fault patches in a characteristic manner. Triggered slip induced by strong shaking from nearby earthquakes can both advance the timing of the release of an accumulating shallow slip deficit and reduce the duration of this slip from days to minutes.

Open Research

Raw Sentinel-1 data used in generating InSAR time series and velocity maps are openly available from Alaska Satellite Facility via `https://search.asf.alaska.edu` (ASF, 2022). GNSS data are from the the Earthscope Geodetic Facility for the Advancement of Geoscience Data Center via `https://www.unavco.org/data/gps-gnss/gps-gnss.html` (EarthScope, 2022). Processed geodetic and field data used in this study are available via Zenodo (`https://zenodo.org/records/10211682`). The seismicity catalogs are available from the Southern California Earthquake Center via `https://scedc.caltech.edu/data` (SCEDC, 2013).

Acknowledgments

We thank Kathryn Materna for thoughtful and engaging discussions regarding the 2023 SHF event. Funding for this study was provided by NSF (GRFP to EV, EAR-1841273 to YF) and NASA (80NSSC22K0506 to YF). YF acknowledges High-End Computing resources from NASA. Funding from USGS and NASA have supported creepmeter maintenance.

Contributions

EV wrote the initial manuscript. All authors contributed to the preparation and revision of the final manuscript. RB processed data from the Colorado creepmeter. PS, JaS, PT, and JoS designed, installed, and maintained the Prague creepmeter and conducted the ERT survey. YF processed the InSAR data. EV analyzed the InSAR data and performed fault inversions. EV, YF, TR, PS, and JoS participated in field work. EV and TR mapped the fault rupture.

304 ## Figures

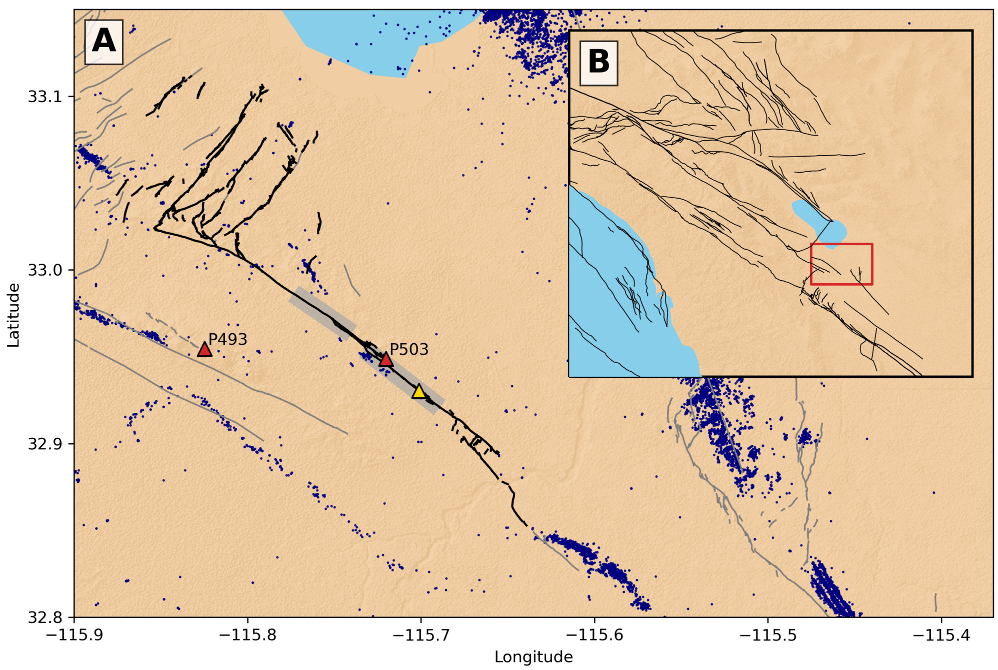

Figure 1. (A) Regional map of the Superstition Hills Fault (SHF). Quaternary faults are shown in gray (USGS, 2020) with the 1987 SHF surface rupture shown in black. The location of the creepmeters is shown with a yellow triangle. GNSS stations P503 and P493 are shown as red triangles. Gray shading indicates the extent of the field survey. Seismicity from 2008-2017 is shown as blue dots (Ross et al., 2019). (B) Regional tectonic setting of the SHF. Major fault traces are plotted in black (Shaw et al., 2015). The area of (A) is shown in red.

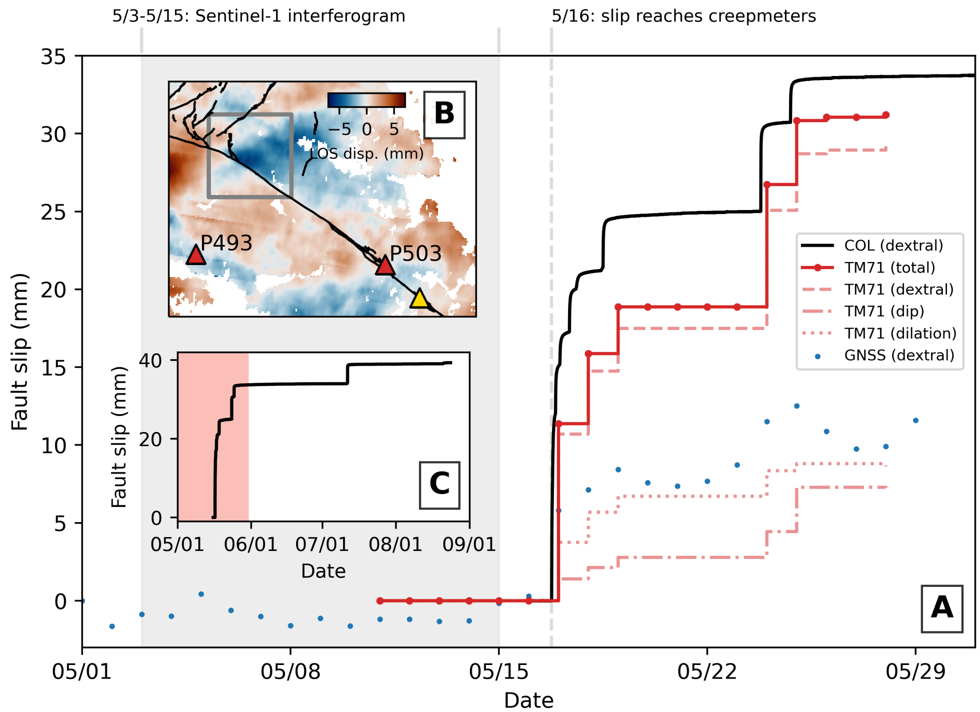

Figure 2. (A) Fault slip during May 2023. Dextral slip measured by COL is shown in black. Red lines show dextral slip (dashed), dip slip (dot-dashed), dilation (dotted), and total fault displacement (solid) from TM71 (circles). Blue dots show the fault-parallel baseline change between stations P503 and P493. Gray shading indicates the epoch of the 3-15 May Sentinel-1 interferogram. (B) 3-15 May Sentinel-1 interferogram showing initial slip on the northern SHF (gray box). (C) Time series of fault slip through August 2023 from COL. Red shading indicates the time span of (A).

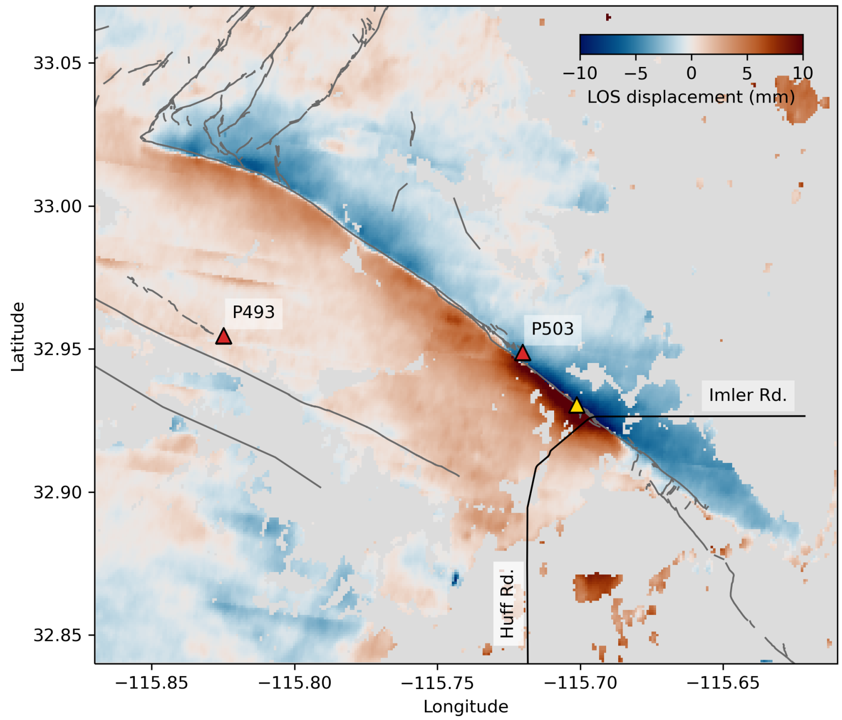

Figure 3. Surface displacements due to 2023 slow slip on the Superstition Hills Fault from Sentinel-1 InSAR analysis. Positive values (red) correspond to motion away from the satellite. Quaternary faults are shown in gray (USGS, 2020). The locations of the creepmeters (yellow triangle) and GNSS stations (red triangles) are also shown.

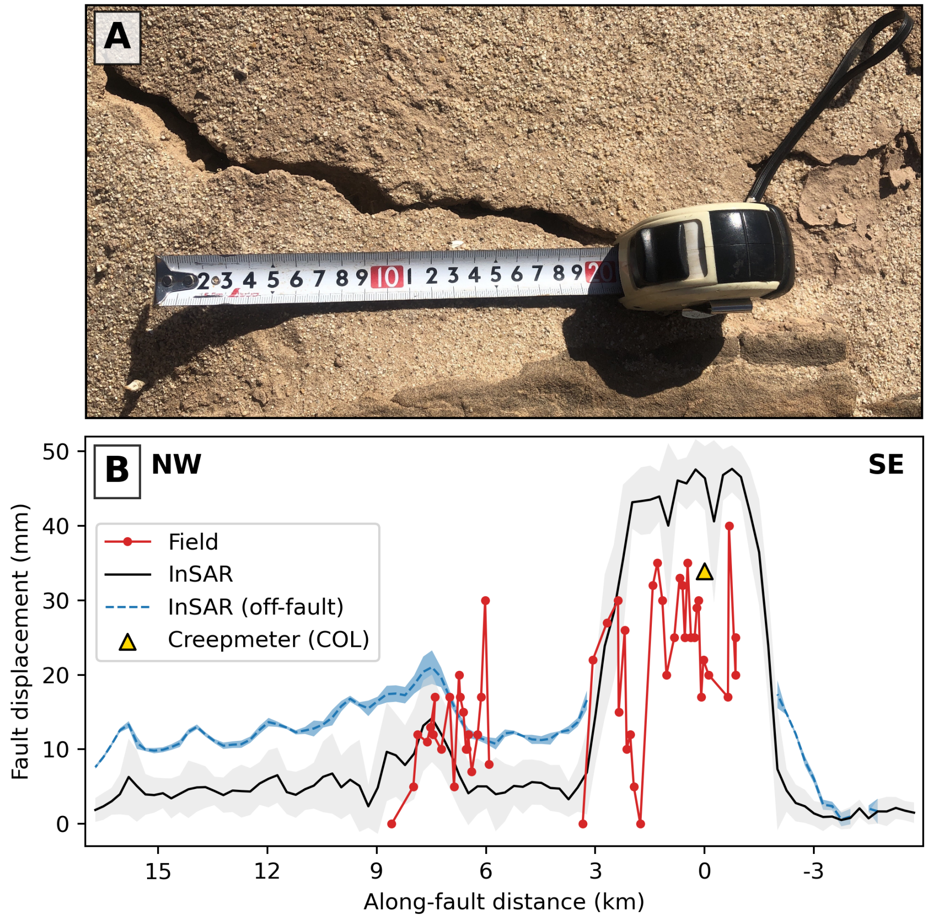

Figure 4. (A) An example surface crack observed during the 11 June 2023 field survey. The measuring tape is in centimeters and is aligned with the local strike. (B) 2023 Surface rupture along the Superstition Hills Fault. Estimated on-fault and maximum off-fault offsets from InSAR are shown with associated shading indicating uncertainty estimates. Red lines indicate the extent of field mapping. The COL creepmeter measurement is from 11 June, while InSAR displacements span 3 May to 8 June. Distances are referenced to the location of the creepmeters.

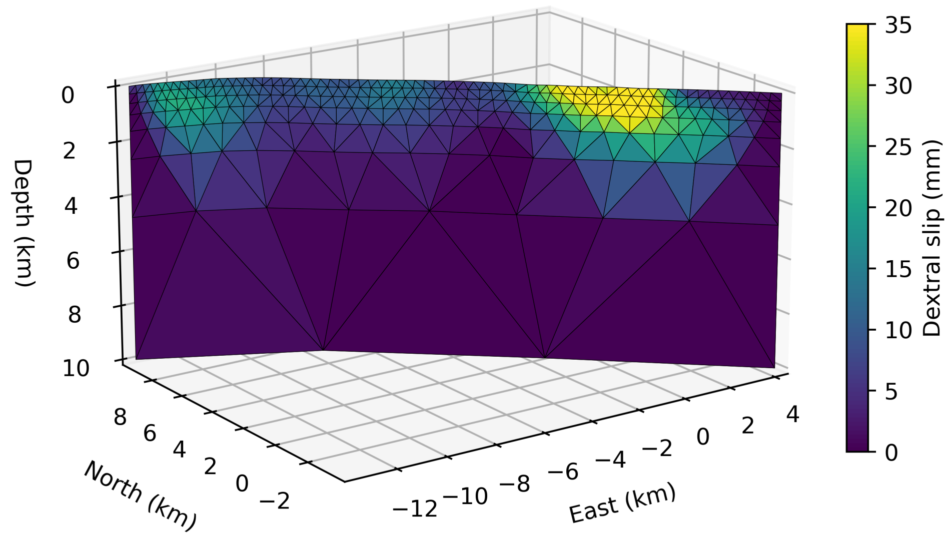

Figure 5. Three-dimensional kinematic model of slip along the Superstition Hills Fault during the 2023 slow-slip event. Fault patch colors correspond to the amplitude of dextral slip. The coordinates are centered at the location of the creepmeters. The moment release associated with this model corresponds to a M_w 5.0 earthquake.

References

Allen, C. R., Wyss, M., Brune, J. N., Grantz, A., & Wallace, R. E. (1972). *Displacements on the Imperial, Superstition Hills, and San Andreas Faults Triggered by teh Borrego Mountain Earthuake.* (Tech. Rep.).

ASF. (2022). *European Space Agency Copernicus Sentinel data [dataset].* Alaska Satellite Facility Distributed Active Archive Center. Retrieved from `https://search.asf.alaska.edu/`

Barbot, S., Fialko, Y., & Bock, Y. (2009). Postseismic deformation due to the M_w 6.0 2004 Parkfield earthquake: Stress-driven creep on a fault with spatially variable rate-and-state friction parameters. *Journal of Geophysical Research*, *114*(B7), B07405.

Barbot, S., Fialko, Y., & Sandwell, D. (2008). Effect of a compliant fault zone on the inferred earthquake slip distribution. *Journal of Geophysical Research*, *113*(B6), B06404.

Bilham, R., & Castillo, B. (2020). The July 2019 Ridgecrest, California, Earthquake Sequence Recorded by Creepmeters: Negligible Epicentral Afterslip and Prolonged Triggered Slip at Teleseismic Distances. *Seismological Research Letters*, *91*(2A), 707–720.

Bilham, R., Ozener, H., Mencin, D., Dogru, A., Ergintav, S., Cakir, Z., . . . others (2016). Surface creep on the North Anatolian fault at Ismetpasa, Turkey, 1944–2016. *J. Geophys. Res.*, *121*(10), 7409–7431.

Bodin, P., Bilham, R., Behr, J., Gomberg, J., & Hudnut, K. W. (1994). Slip triggered on southern California faults by the 1992 Joshua Tree, Landers, and Big Bear earthquakes. *Bulletin of the Seismological Society of America*, *84*(3), 806–816.

Brooks, B. A., Minson, S. E., Glennie, C. L., Nevitt, J. M., Dawson, T., Rubin, R., . . . others (2017). Buried shallow fault slip from the South Napa earthquake revealed by near-field geodesy. *Science advances*, *3*, e1700525.

Donnellan, A., Parker, J., Hensley, S., Pierce, M., Wang, J., & Rundle, J. (2014). UAVSAR observations of triggered slip on the Imperial, Superstition Hills, and East Elmore Ranch Faults associated with the 2010 M 7.2 El Mayor-Cucapah earthquake. *Geochemistry, Geophysics, Geosystems*, *15*(3), 815–829.

Dragert, H., Wang, K., & James, T. S. (2001). A Silent Slip Event on the Deeper

Cascadia Subduction Interface. *Science*, *292*(5521), 1525–1528.

EarthScope. (2022). *Global navigation satellite system position solutions [dataset].* Geodetic Facility for the Advancement of Geoscience. Retrieved from https://www.unavco.org/data/gps-gnss/gps-gnss.html

Fialko, Y. (2006). Interseismic strain accumulation and the earthquake potential on the southern San Andreas fault system. *Nature*, *441*(7096), 968–971.

Fialko, Y., Sandwell, D., Agnew, D., Simons, M., Shearer, P., & Minster, B. (2002). Deformation on Nearby Faults Induced by the 1999 Hector Mine Earthquake. *Science*, *297*(5588), 1858–1862.

Fialko, Y., Sandwell, D., Simons, M., & Rosen, P. (2005). Three-dimensional deformation caused by the Bam, Iran, earthquake and the origin of shallow slip deficit. *Nature*, *435*(7040), 295–299.

Field, E. H., Arrowsmith, R. J., Biasi, G. P., Bird, P., Dawson, T. E., Felzer, K. R., ... others (2014). Uniform California Earthquake Rupture Forecast, version 3 (UCERF3) The time-independent model. *Bull. Seism. Soc. Am.*, *104*, 1122–1180.

Field, E. H., Biasi, G. P., Bird, P., Dawson, T. E., Felzer, K. R., Jackson, D. D., ... Zeng, Y. (2015). Long-Term Time-Dependent Probabilities for the Third Uniform California Earthquake Rupture Forecast (UCERF3). *Bulletin of the Seismological Society of America*, *105*(2A), 511–543.

Fuis, G. S. (1982). Displacement on the Superstition Hills fault triggered by the earthquake. *U.S. Geologic Survey Professional Paper*, *1254*, 145–154.

Hauksson, E., Stock, J., Bilham, R., Boese, M., Chen, X., Fielding, E. J., ... Yang, W. (2013). Report on the August 2012 Brawley Earthquake Swarm in Imperial Valley, Southern California. *Seismological Research Letters*, *84*(2), 177–189.

Heflin, M., Donnellan, A., Parker, J., Lyzenga, G., Moore, A., Ludwig, L. G., ... Pierce, M. (2020). Automated Estimation and Tools to Extract Positions, Velocities, Breaks, and Seasonal Terms From Daily GNSS Measurements: Illuminating Nonlinear Salton Trough Deformation. *Earth and Space Science*, *7*(7), e2019EA000644.

Hudnut, K. W., & Sieh, K. E. (1989). Behavior of the Superstition Hills fault during the past 330 years. *Bulletin of the Seismological Society of America*, *79*(2), 304–329.

Jin, Z., Fialko, Y., Zubovich, A., & Schöne, T. (2022). Lithospheric Deformation Due To the 2015 M7.2 Sarez (Pamir) Earthquake Constrained by 5 years of Space Geodetic Observations. *Journal of Geophysical Research: Solid Earth*, *127*(4), e2021JB022461.

Kaneko, Y., Fialko, Y., Sandwell, D. T., Tong, X., & Furuya, M. (2013). Interseismic deformation and creep along the central section of the North Anatolian Fault (Turkey): InSAR observations and implications for rate-and-state friction properties. *Journal of Geophysical Research: Solid Earth*, *118*(1), 316–331.

Klimeš, J., Rowberry, M. D., Blahůt, J., Briestenský, M., Hartvich, F., Košťák, B., … Štěpančíková, P. (2012). The monitoring of slow-moving landslides and assessment of stabilisation measures using an optical–mechanical crack gauge. *Landslides*, *9*(3), 407–415.

Kohler, W. M., & Fuis, G. S. (1986). Travel-time, time-term, and basement depth maps for the Imperial Valley region, California, from explosions. *Bulletin of the Seismological Society of America*, *76*(5), 1289–1303.

Košťák, B. (1969). A new device for in-situ movement detection and measurement. *Experimental Mechanics*, *9*(8), 374–379.

LaBonte, A., Brown, K., & Fialko, Y. (2009). Hydrogeologic detection and finite-element modeling of a slow-slip event in the Costa Rica prism toe. *J. Geophys. Res.*, *114*, B00A02.

Li, V. C., & Rice, J. (1987). Crustal Deformation in Great California Earthquake Cycles. *J. Geophys. Res.*, *92*, 11533–11551.

Lindsey, E. O., & Fialko, Y. (2016). Geodetic constraints on frictional properties and earthquake hazard in the Imperial Valley, Southern California. *Journal of Geophysical Research: Solid Earth*, *121*(2), 1097–1113.

Lindsey, E. O., Fialko, Y., Bock, Y., Sandwell, D. T., & Bilham, R. (2014). Localized and distributed creep along the southern San Andreas Fault. *Journal of Geophysical Research: Solid Earth*, *119*(10), 7909–7922.

Lindsey, E. O., Sahakian, V. J., Fialko, Y., Bock, Y., Barbot, S., & Rockwell, T. K. (2014). Interseismic Strain Localization in the San Jacinto Fault Zone. *Pure and Applied Geophysics*, *171*(11), 2937–2954.

Louie, J. N., Johnson, D. C., Haase, P. C., & Cohn, S. N. (1985). Fault Slip in

Southern California. *Bulletin of the Seismological Society of America*, *75*(3), 811–833.

Marone, C. J., Scholtz, C. H., & Bilham, R. (1991). On the mechanics of earthquake afterslip. *Journal of Geophysical Research: Solid Earth*, *96*(B5), 8441–8452.

Martí, X., Rowberry, M. D., & Blahůt, J. (2013). A MATLAB® code for counting the moiré interference fringes recorded by the optical-mechanical crack gauge TM-71. *Computers & Geosciences*, *52*, 164–167.

Nof, R. N., Ziv, A., Doin, M.-P., Baer, G., Fialko, Y., Wdowinski, S., ... Bock, Y. (2012). Rising of the lowest place on Earth due to Dead Sea water-level drop: Evidence from SAR interferometry and GPS. *J. Geophys. Res.*, *117*(B5).

Parker, J., Donnellan, A., Bilham, R., Ludwig, L. G., Wang, J., Pierce, M., ... Jänecke, S. (2021). Buried Aseismic Slip and Off-Fault Deformation on the Southernmost San Andreas Fault Triggered by the 2010 El Mayor Cucapah Earthquake Revealed by UAVSAR. *Earth and Space Science*, *8*(8).

Pearse, J., & Fialko, Y. (2010). Mechanics of active magmatic intraplating in the Rio Grande Rift near Socorro, New Mexico. *J. Geophys. Res.*, *115*, B07413.

Ross, Z. E., Trugman, D. T., Hauksson, E., & Shearer, P. M. (2019). Searching for hidden earthquakes in Southern California. *Science*, *364*, 767–771.

Rymer, M. J. (2000). Triggered Surface Slips in the Coachella Valley Area Associated with the 1992 Joshua Tree and Landers, California, Earthquakes. *Bulletin of the Seismological Society of America*, *90*(4), 832–848.

Rymer, M. J., Boatwright, J., Seekins, L. C., Yule, D., & Liu, J. (2002). Triggered Surface Slips in the Salton Trough Associated with the 1999 Hector Mine, California, Earthquake. *Bulletin of the Seismological Society of America*, *92*(4), 1300–1317.

SCEDC. (2013). *Southern California Earthquake Data Center [dataset].* Caltech. doi: https://doi.org/10.7909/C3WD3XH1

Sharp, R. V. (1967). San Jacinto fault zone in the Peninsular Ranges of southern California. *Geol. Soc. Am. Bull.*, *78*, 705–730.

Sharp, R. V., Budding, K. E., Boatwright, J., Ader, M. J., Bonilla, M. G., Clark, M. M., ... Sims, J. D. (1989). Surface faulting along the Superstition Hills fault zone and nearby faults associated with the earthquakes of 24 November 1987. *Bulletin of the Seismological Society of America*, *79*(2), 252–281.

Sharp, R. V., Rymer, M. J., & Lienkaemper, J. J. (1986). Surface displacement on the Imperial and Superstition Hills faults triggered by the Westmorland, California, earthquake of 26 April 1981. *Bulletin of the Seismological Society of America*, *76*(4), 949–965.

Shaw, J. H., Plesch, A., Tape, C., Suess, M. P., Jordan, T. H., Ely, G., … Munster, J. (2015). Unified Structural Representation of the southern California crust and upper mantle. *Earth and Planetary Science Letters*, *415*, 1–15.

Tymofyeyeva, E., & Fialko, Y. (2015). Mitigation of atmospheric phase delays in InSAR data, with application to the eastern California shear zone. *Journal of Geophysical Research: Solid Earth*, *120*(8), 5952–5963.

Tymofyeyeva, E., & Fialko, Y. (2018). Geodetic Evidence for a Blind Fault Segment at the Southern End of the San Jacinto Fault Zone. *Journal of Geophysical Research: Solid Earth*, *123*(1), 878–891.

Tymofyeyeva, E., Fialko, Y., Jiang, J., Xu, X., Sandwell, D., Bilham, R., … Moafipoor, S. (2019). Slow Slip Event On the Southern San Andreas Fault Triggered by the 2017 Mw 8.2 Chiapas (Mexico) Earthquake. *Journal of Geophysical Research: Solid Earth*, *124*(9), 9956–9975.

USGS. (2020). *Quaternary Fault and Fold Database for the Nation.*

Vavra, E. J., Qiu, H., Chi, B., Share, P.-E., Allam, A., Morzfeld, M., … Fialko, Y. (2023). Active dipping interface of the southern San Andreas fault revealed by space geodetic and seismic imaging. *Journal of Geophysical Research: Solid Earth*, *128*(11), e2023JB026811.

Wald, D. J., Helmberger, D. V., & Hartzell, S. H. (1990). Rupture process of the 1987 superstition hills earthquake from the inversion of strong-motion data. *Bulletin of the Seismological Society of America*, *80*(5), 1079–1098.

Wallace, L. M. (2020). Slow Slip Events in New Zealand. *Annual Review of Earth and Planetary Sciences*, *48*(1), 175–203.

Wei, M., Liu, Y., Kaneko, Y., McGuire, J. J., & Bilham, R. (2015). Dynamic triggering of creep events in the Salton Trough, Southern California by regional M 5.4 earthquakes constrained by geodetic observations and numerical simulations. *Earth and Planetary Science Letters*, *427*, 1–10.

Wei, M., Sandwell, D., & Fialko, Y. (2009). A silent M_w 4.7 slip event of October 2006 on the Superstition Hills fault, southern California. *Journal of Geophysi-*

cal Research, *114* (B7), B07402.

Wei, M., Sandwell, D., Fialko, Y., & Bilham, R. (2011). Slip on faults in the Imperial Valley triggered by the 4 April 2010 Mw 7.2 El Mayor-Cucapah earthquake revealed by InSAR. *Geophysical Research Letters*, *38* (1).

Williams, P. L., & Magistrale, H. W. (1989). Slip along the Superstition Hills fault associated with the 24 November 1987 Superstition Hills, California, earthquake. *Bulletin of the Seismological Society of America*, *79* (2), 390–410.

Zebker, H. A., Rosen, P. A., & Hensley, S. (1997). Atmospheric effects in interferometric synthetic aperture radar surface deformation and topographic maps. *Journal of Geophysical Research: Solid Earth*, *102* (B4), 7547–7563.

Figure 1.

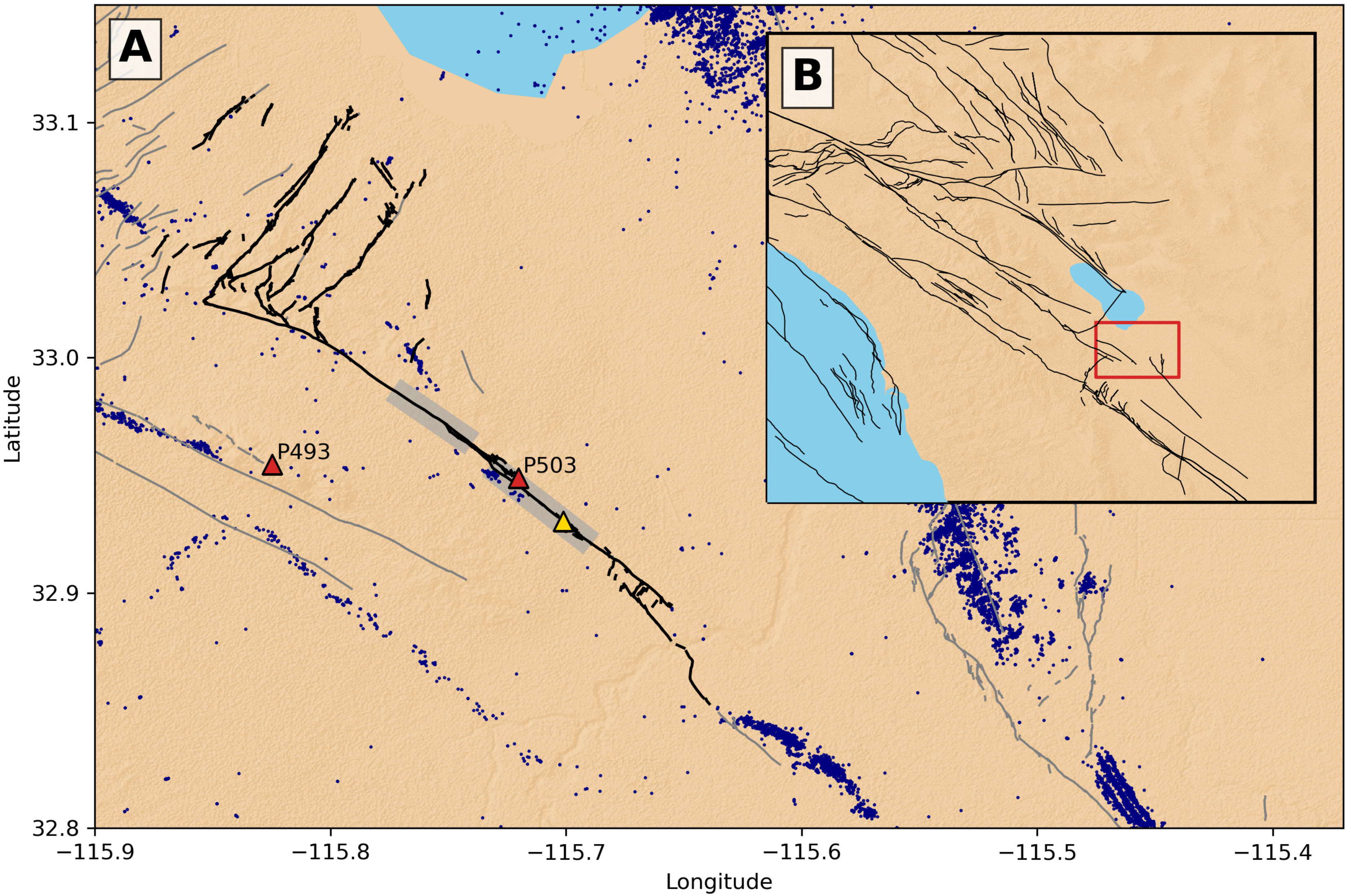
A
B
P493
P503
33.1
33.0
32.9
32.8
Latitude
−115.9
−115.8
−115.7
−115.6
−115.5
−115.4
Longitude

Figure 2.

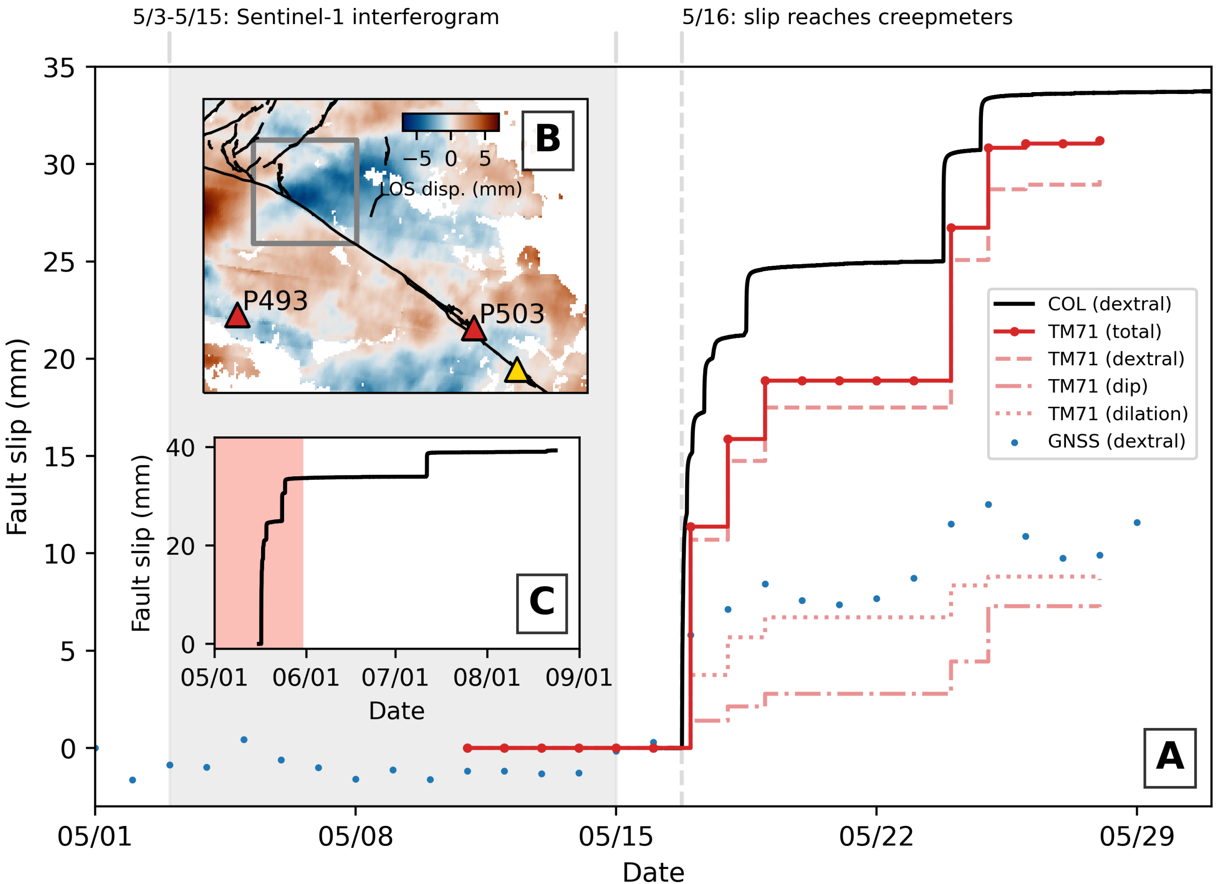

5/3-5/15: Sentinel-1 interferogram
5/16: slip reaches creepmeters
Fault slip (mm)
35
30
25
20
15
10
5
0
05/01
05/08
05/15
05/22
05/29
Date
−5 0 5
LOS disp. (mm)
B
P493
P503
COL (dextral)
TM71 (total)
TM71 (dextral)
TM71 (dip)
TM71 (dilation)
GNSS (dextral)
40
20
0
05/01
06/01
07/01
08/01
09/01
C
A

Figure 3.

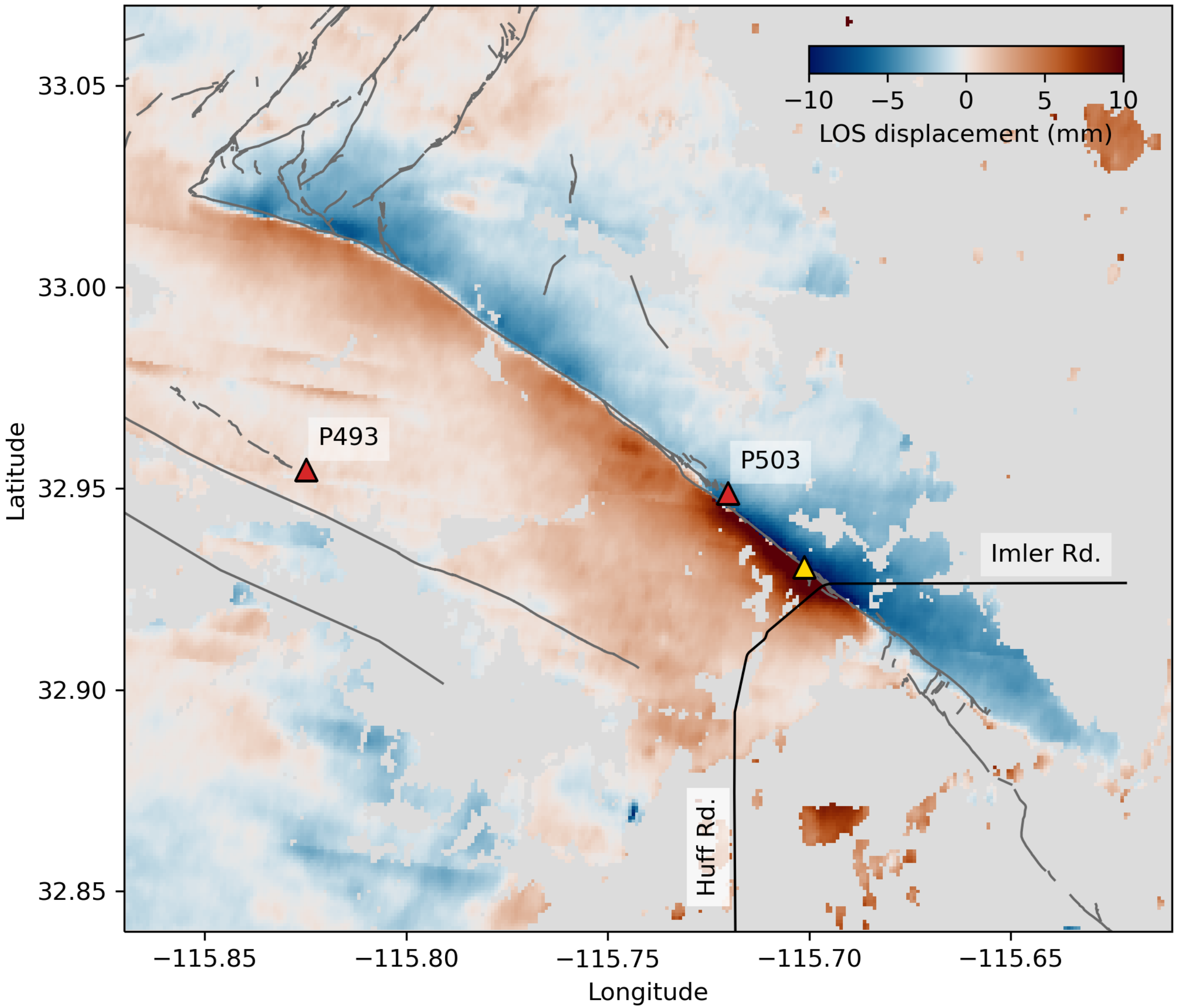

−10
−5
0
5
10
LOS displacement (mm)
33.05
33.00
32.95
32.90
32.85
Latitude
−115.85
−115.80
−115.75
−115.70
−115.65
Longitude
P493
P503
Imler Rd.
Huff Rd.

Figure 4.

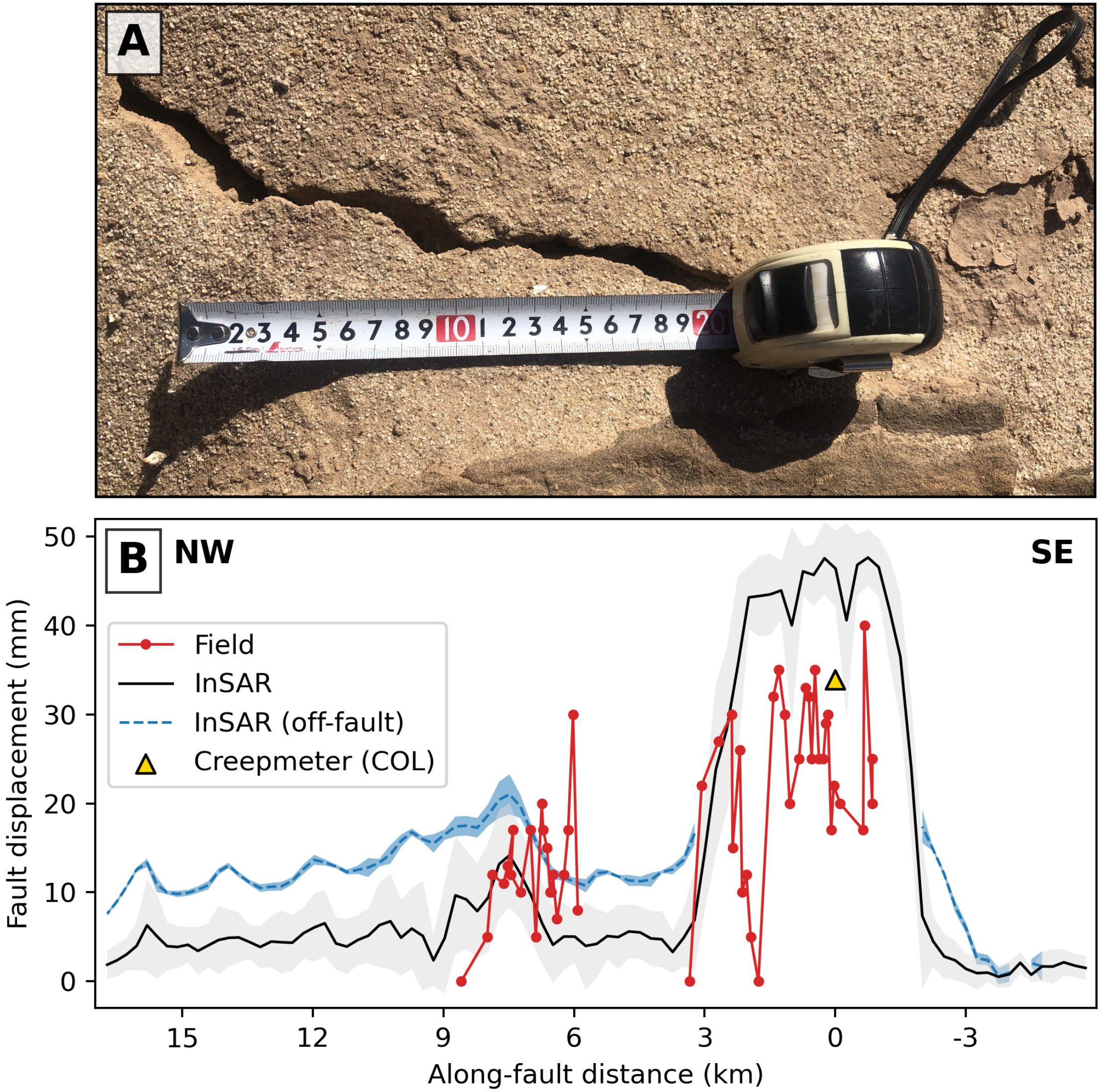
A
2 3 4 5 6 7 8 9 10 1 2 3 4 5 6 7 8 9 20
B
NW
SE
Field
InSAR
InSAR (off-fault)
Creepmeter (COL)
Fault displacement (mm)
50
40
30
20
10
0
15
12
9
6
3
0
-3
Along-fault distance (km)

Figure 5.

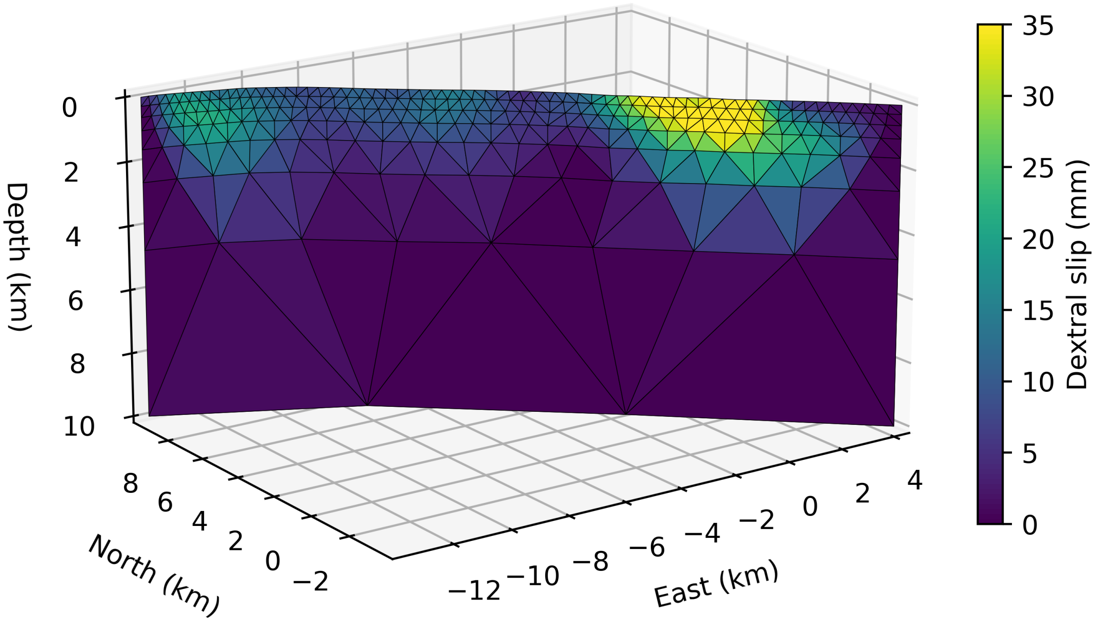

Depth (km)
0
2
4
6
8
10
North (km)
8
6
4
2
0
−2
East (km)
−12
−10
−8
−6
−4
−2
0
2
4
Dextral slip (mm)
35
30
25
20
15
10
5
0

Supporting Information for "Characteristic Slow-Slip Events on the Superstition Hills Fault, Southern California"

Ellis J. Vavra[1], Yuri Fialko[1], Thomas Rockwell[2], Roger Bilham[3], Petra Štěpančíková[4], Jakub Stemberk[4], Petr Tábořík[4], Josef Stemberk[4]

[1]Institute of Geophysics and Planetary Physics, Scripps Institution of Oceanography, University of California, San Diego, La Jolla, CA, USA

[2]Department of Geological Sciences, San Diego State University, San Diego, CA, USA

[3]Cooperative Institute for Research in Environmental Sciences, University of Colorado, Boulder, Boulder, CO, USA

[4]Institute of Rock Structure and Mechanics, Czech Academy of Sciences, Prague, Czech Republic

Contents

Introduction

This document contains supplementary text and figures referenced in the main text.

Text S1: Description of the Creepmeters

The Colorado (COL) creepmeter consists of a 6-m-long, 4-mm-diameter pultruded carbon rod anchored to the east side of the fault, which crosses the fault at 30° within a 2 cm internal diameter plastic conduit (Bilham & Castillo, 2020). The instrument is thereby anchored ±1.5m from the fault trace. Its free end on the west side of the fault is held in tension by a 0.15-mm-diameter, 19-strand, nylon-coated, stainless-steel wire spooled on a 1 N constant-tension spring motor. The wire is wrapped once around the shaft of a low friction rotary Hall sensor causing the shaft to rotate in response to fault slip. Each complete rotation of the shaft results in a 4.5 V linear voltage change (corresponding to ∼11.5 mm of dextral fault slip) that resets to zero at a 360°-0 transition, thereby permitting an extended measurement range of 1.3 m limited by the length of the

Corresponding author: Ellis J. Vavra, evavra@ucsd.edu

spooled wire. The output is measured once per minute to a precision of 3 µm. The 39 mm extended creep event resulted in more than two complete shaft rotations that have been removed in Figure 2. In the 13 years prior to the 2023 slip event the creepmeter had recorded a linear featureless fault slip rate of 0.3 mm/year.

The TM-71 opto-mechanical creepmeter measures dip-slip, strike-slip, dilation, and rotation between two blocks separated by a discontinuity at daily intervals (Košťák, 1969; Klimeš et al., 2012; Martí et al., 2013). Total vector of fault displacement u is then calculated based on these components:

$$u = \sqrt{u_{strike-slip}^2 + u_{dip-slip}^2 + u_{dilation}^2} \tag{1}$$

The instrument uses optical interference that appears when spirals on two glass sheets slide over one another, and characteristic Moiré interference occur (Kostak & Popp, 1966; Martí et al., 2013). The interference effect can be transformed into a metric system through the number of strips and axis of symmetry (Kostak & Popp, 1966). The value of displacement between the centres of glass sheets is determined by the number of interference strips, and the direction of displacement is shown by the main axis of symmetry of the optical effect. All possible relative movements of the blocks are measured once per day to a precision of 1 μm. The relative rotation between two blocks are measured to a precision of $> 3.2 \times 10^4$ rad ($\approx 0.018°$).

Text S3: InSAR offset estimation procedure

Surface offsets along the trace of the SHF are the primary dataset documenting past coseismic and aseismic fault ruptures (e.g., Allen et al., 1972; Sharp et al., 1986; Rymer et al., 2002; Wei et al., 2011). We estimate surface offsets for the 2023 SSE by averaging InSAR pixels on opposite sides of the mapped fault trace at regular intervals. We select fault-perpendicular 10 km-by-250 m swaths at 250 m intervals along the fault and difference the means of bins of pixels on either side of the fault to estimate offsets. Some large outlier pixels exist, in particular near the highly localized slip patch near Imler Road (Figures 3 & 4), due to decorrelation and/or unwrapping errors. To identify outliers, we utilize the z-score,

$$Z_i = \frac{x_i - \mu}{\sigma} \tag{2}$$

which describes deviation of a value x_i from the mean μ with respect to the standard deviation σ. We modify Equation 1 in order to emphasize the detection of outlier data points by computing the mean $\hat{\mu}$ and standard deviation $\hat{\sigma}$ of the data x_j for $j \neq i$, resulting in the adjusted z-score $\hat{Z}_i = \frac{x_i - \hat{\mu}}{\hat{\sigma}}$ which is exaggerated compared to Z_i due to the relative changes in the mean $\hat{\mu}$ and standard deviation $\hat{\sigma}$.

Initially, we bin data within ± 200 m of the fault and compute $\hat{Z}_i$ for all pixels in each bin. We then fit a straight line to each group of pixels with $\hat{Z}_i \leq 1$ to determine if slip is localized or distributed. If the signs of the slopes are the same, slip is determined to be distributed across the fault trace; if the signs are opposite, then slip is discontinuous. Since we are only interested in removing extreme outliers associated with high amplitude, localized slip, we compute fault offsets simply using all pixels within ± 100 m bins if distributed slip is identified. If slip is localized, we omit pixels with $\hat{Z}_i > 1$ and use the means and standard deviations of the remaining pixels to estimate fault offsets and their uncertainties. This procedure produces near-field (i.e. "on-fault") surface offset estimates which are suitable for comparison with field and creepmeter measurements of observed fault slip (although there still lie differences in measurement aperture which bias each observation). However, examination of individual profiles (Figure S4) shows that along much of the northern portion of the fault, where deformation is distributed, maximum deformation occurs off-fault.

To quantify the "maximum offsets" at the surface for distributed deformation, we identify the shear zone width using the gradients of the displacements and compute offsets at the edges of the shear zone. We smooth the profiles using a Savitsky-Golay filter (window of 35 and polynomial order of 3), interpolate the smoothed profiles to 10 m resolution, and then compute the displacement gradient du/dx of the smoothed and interpolated profiles. We estimate the width of the distributed shear zone by finding the nearest-fault location where $du/dx = 0$ on either side of the fault. We place a maximum shear zone width of 2000 m, determined by manual inspection of the profiles, in order to avoid erroneous estimates due to residual atmospheric noise. To estimate the maximum off-fault displacements, we use the mean of original InSAR pixels within ± 100 m of the identified shear zone edges. We also estimate uncertainties by computing the standard deviations within the same bins. Results for both the on-fault and off-fault displacements are shown in Figure 4B.

Text S4: Finite Fault Inversion Procedure

We use the Sentinel-1A InSAR measurements of slip during the 2023 SSE to invert for the 3D distribution of slip along the SHF. We mapped a simplified version of the active SHF through combination of its representation in the USGS Quaternary fault database (USGS, 2020) and the observed surface displacements due to 2023 slip (Figure 3). We generate a triangular mesh by assuming a vertical fault geometry and tessellating triangular elements 10 km depth. The minimum element dimensions are 0.25-0.3 km t the surface and increase geometrically with depth. The resulting mesh has 492 elements. From the fault mesh geometry, we compute fault Greens functions for surface displacements using a Python implementation for triangular dislocation elements (Nikkhoo & Walter, 2015) from Ben Thompson (`https://github.com/tbenthompson/cutde`).

Since the fault geometry (and thus Greens functions) is fixed, the resulting inverse problem is linear and over-determined. We solve for the optimal slip distribution along the fault using least squares. We generate Greens functions for dextral fault slip and project them to the satellite line-of-sight (LOS). We add a slip-smoothness constraint that uses first-differences between neighboring TDEs to limit sharp changes in the slip distribution (e.g., Aster et al., 2018). We also include a soft zero-slip boundary condition to enforce the assumption that slip tapers to zero at the edges of the rupture. The resulting set of linear equations is

$$\begin{bmatrix} \boldsymbol{G} \\ \mu\boldsymbol{R} \\ \eta\boldsymbol{L} \end{bmatrix} \begin{bmatrix} \boldsymbol{m} \end{bmatrix} = \begin{bmatrix} \boldsymbol{d} \\ \boldsymbol{0} \\ \boldsymbol{0} \end{bmatrix} \tag{3}$$

where $\boldsymbol{G}$ are the LOS-projected Greens functions, $\boldsymbol{R}$ is the first-difference smoothness operator, $\boldsymbol{L}$ is the zero-slip boundary operator (applied to TDEs at the bottom and lateral edges of the fault, with the exception of corner elements at the surface), μ and η are weights applied to the smoothness and zero-slip regularization terms, respectively, $\boldsymbol{d}$ is composed of InSAR LOS measurements, and $\boldsymbol{m}$ is the modelled slip distribution. We solve Equation 2 for $\boldsymbol{m}$ using least-squares with a positivity constraint to enforce dextral-only slip.

To determine values for the regularization weights μ and η that appropriately balance model complexity (i.e. slip heterogeneity) and smoothness, we perform a grid search over $10^{-3} - 10^{3}$ for both parameters (Figure S5). We use 20 samples for each parameter, resulting in 400 models. We find large increases in the root-mean-square (RMS) of model residuals for $\mu > 5 \times 10^1$ (Figure S5). Visual inspection of associated models shows systematic residuals with fault-like patterns, suggesting $\mu > 5 \times 10^1$ generates unrealistically smooth slip distributions. For models with $\mu < 5 \times 10^1$, there is little change in RMS with increased η. This suggests that little slip near the edges of the model domain is required to fit the data, which is consistent with slip being limited to the extent of shallow sediments (Kohler & Fuis, 1986). Our preferred model (blue dot in Figure S5) uses $\mu = 0.7$ and $\eta = 1.4$ (Figure 5)

To improve the computational efficiency of our inversions without reducing the quantitative information in our dataset, we down-sample the full InSAR displacement field using a quad-tree algorithm (Jonsson, 2002; Simons, 2002). Thus, in all inversions, $\boldsymbol{d}$ is composed of down-sampled data rather than the full-resolution InSAR pixels. We allow the size of the quad-tree cells to approach full resolution ($\sim$ 100 m) where gradients are high (i.e. near the fault trace) and place a maximum size of 2 km where gradients are low (Figure S6).

To avoid oversampling regions of high-frequency noise or residual troposphere noise, we use an iterative model-based approach (Wang & Fialko, 2018). First, we generate an initial displacement field using a prescribed synthetic slip distribution. We then apply the quad-tree algorithm to the initial displacement field model in order to obtain a first-order approximation of the appropriate sampling distribution, with dense sampling near the fault trace and more sparse sampling in the far-field. For the grid search, we only use the initial sampling distribution in order to accurately compare model performance across the ranges of regularization parameters μ and η. After determining reasonable values for μ and η, we apply the quad-tree sampling obtained from the starting model to the real data (Figures 3 & S6) and repeat the process several times, each time re-sampling based on the previous model prediction. To obtain our final preferred model, we use three iterations; Figure S6 shows the final down-sampled dataset.

Text S5: Possible Triggering of the 2023 SSE

While most documented SHF slip events are triggered by regional earthquakes, there is no clear connection to seismicity for the 2023 or 2006 SSEs (Wei et al., 2009). We investigated both regional and global seismicity to confirm whether the 2023 event was spontaneous or dynamically triggered. Over 29-30 April 2023, four M_w 4+ earthquakes occurred in the Salton Trough and within 40 km of the nucleation site of the 2023 SSE (Figure S7). The first event occurred at the Heber geothermal field and a sequence of three $M_w \approx 4.3$ events followed at the Salton Sea geothermal field approximately 18 hours after the Heber event. We inspected a Sentinel-1 interferogram spanning 22 April 2023 - 3 May 2023 and found no discernible deformation along the SHF which may have been instantaneously triggered by dynamic stresses associated with any of the late-April 2023 Salton Trough events. While perturbations to the pore pressure state of the SHF due to these events (e.g., Brodsky, 2003) may have contributed to the subsequent occurrence of the 2023 SSE, we find no evidence for fault slip prior to 3 May 2023.

Several additional regional and global earthquakes occurred during the 3-15 May 2023 Sentinel-1 interferogram epoch. An aftershock of the M_w 4.1 Heber event occurred on 6 May, which was the largest event in the Salton Trough between 3-15 May (Figure S7). In addition, a M_w 6.4 event in Japan on 4 May, a M_w 7.6 event near Samoa on 10 May, and a M_w 5.2 near Lassen, CA on 12 May occurred within the timeframe of the interferogram. We suggest dynamic triggering is unlikely to have initiated the 2023 event as slip during previous triggered events on the SHF only occurred during and immediately after the passing seismic waves, resulting in a step-like signal (Wei et al., 2011). In addition, the relatively stronger ground shaking less than two weeks prior due to the local M_w 4+ events did not initiate slip on the SHF. While prolonged SSEs have been shown to occur on the Southern San Andreas Fault in response to teleseismic surface waves (Tymofyeyeva et al., 2019), the similarity in the temporal history of the 2023 SSE with the 2006 SSE, and lack thereof with respect to observed dynamically triggered SHF events leads us to suggest that the 2023 event was most likely spontaneous.

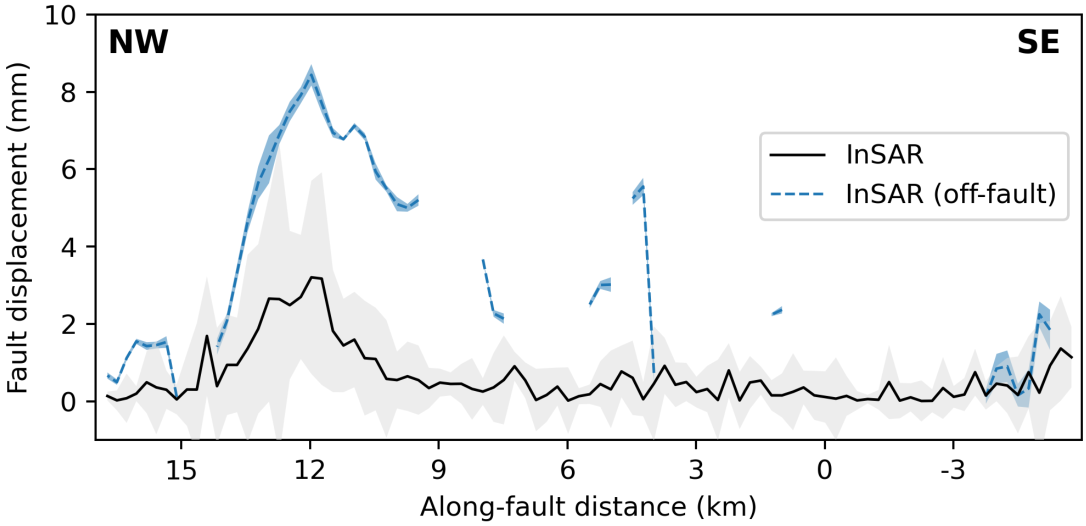

Figure S1. Surface offsets calculated from a Sentinel-1 interferogram spanning 3-15 May 2023. Maximum slip of ∼5-8 mm is observed at about ∼14 km to ∼10 km along the fault. Along-strike distances are referenced to the location of the creepmeters. Detected slip outside of ∼15 km to ∼8 km is likely due to residual atmospheric noise (see Figures 2B and S4).

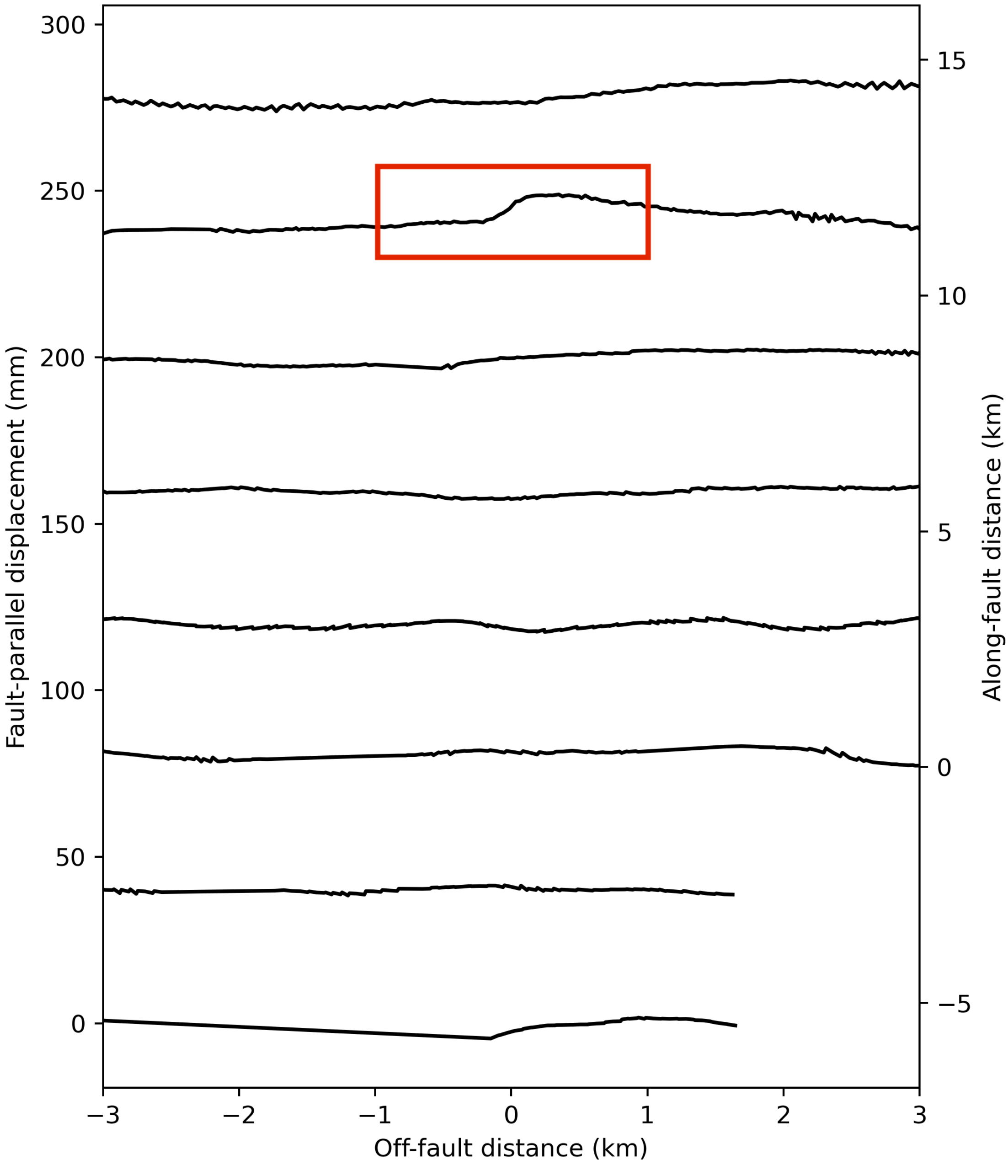

Figure S2. Example displacement profiles at 3 km intervals for an interferogram spanning 3-15 May 2023. The red box indicates distributed surface deformation due to fault slip ∼11 km north of the creepmeters. To improve visualization, this figure uses 10 km-by-100 m profiles at 3 km intervals instead of the profiles used in computing fault offsets (see Text S3).

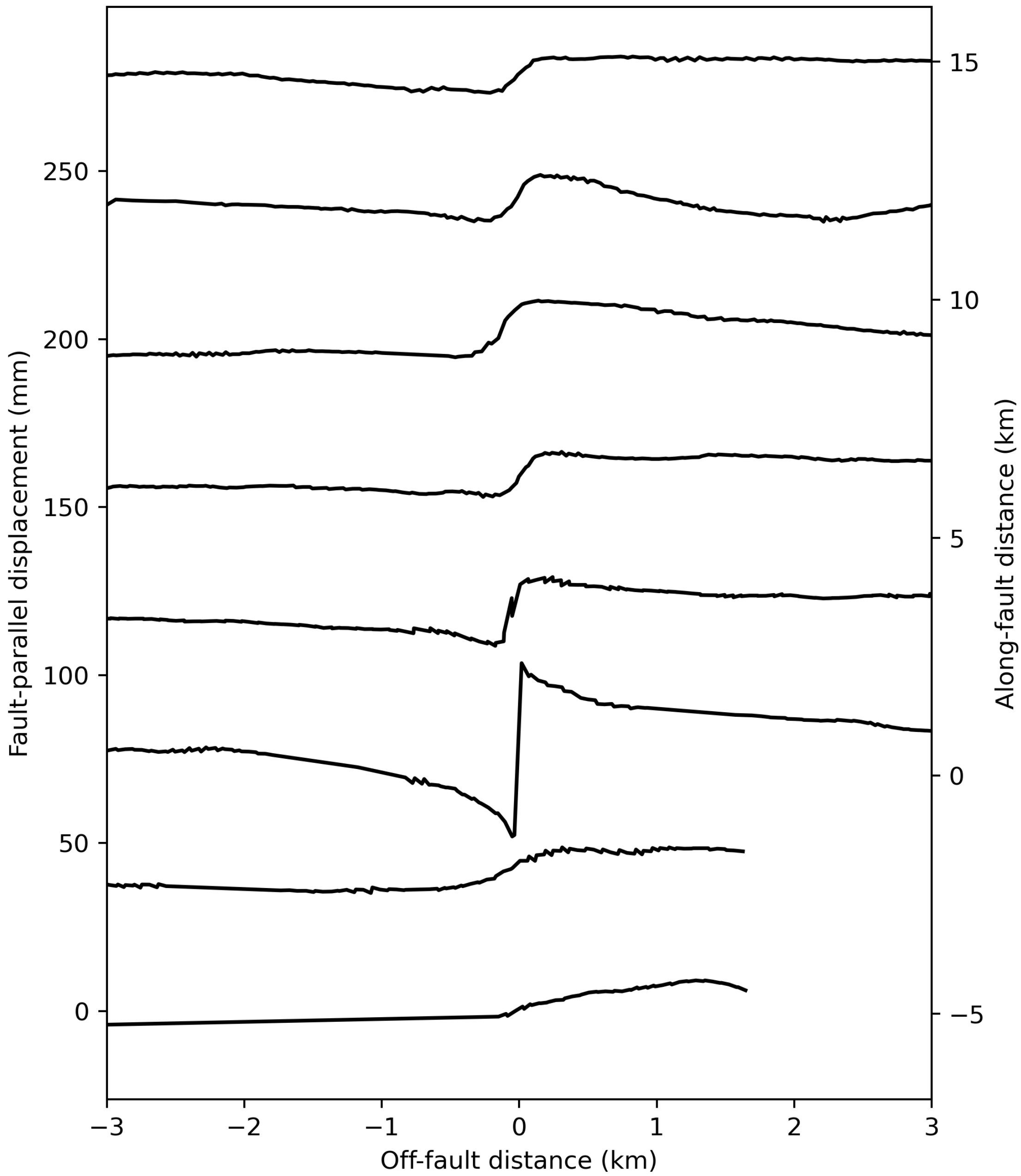

Figure S3. Same as Figure S3 but for 3 May 2023 to 8 June 2023 (same timeframe as Figure 4). Variations in slip localization at the surface is apparent, with highly localized deformation only occurring within several km of the creepmeters ($y \approx -2 - 3$ km; Figure 4).

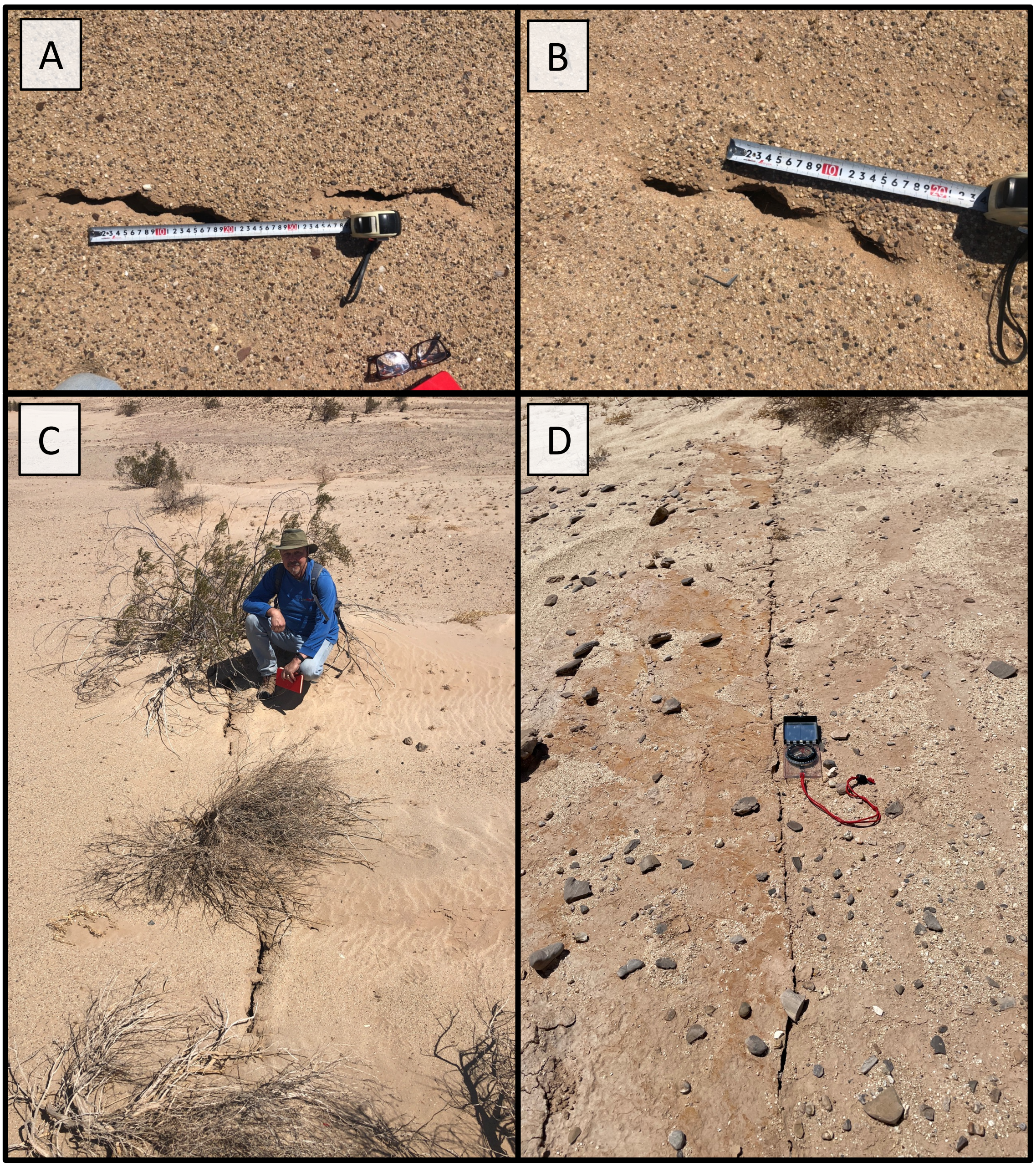

Figure S4. Additional photos of the 2023 surface rupture from the 11 June 2023 field survey.

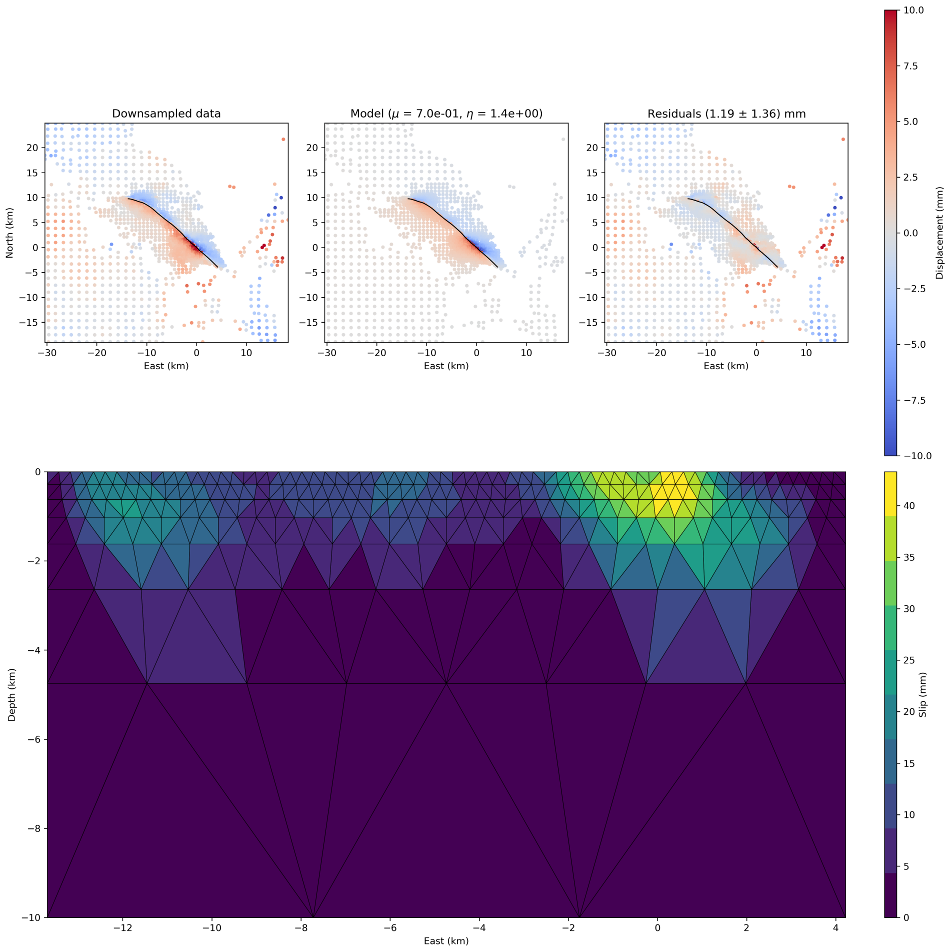

Figure S5. Quad-tree down-sampling and slip distribution associated with the preferred finite fault model. The top row shows InSAR data, model prediction, and resiuals for the the final iteration of quad-tree down-sampling (see Text S4). The bottom panel shows a 2D view of the inverted slip distribution (same model as Figure 5).

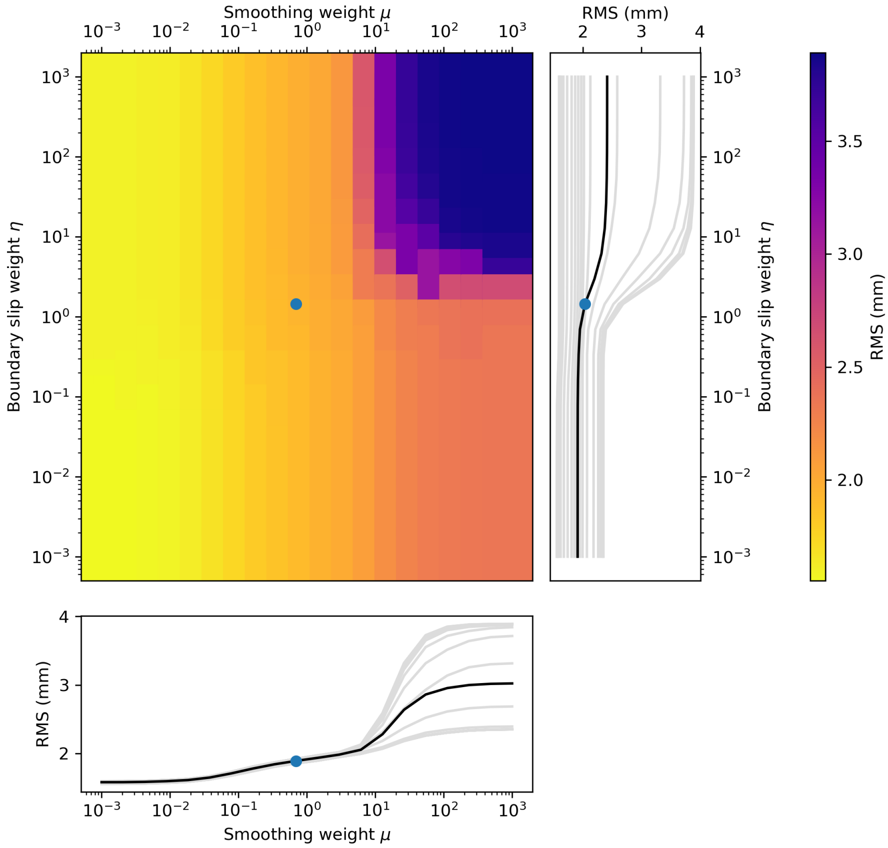

Figure S6. Grid search results over values of smoothness μ and edge slip η constraints. Values between 10^{-3} – 10^{3} were tested for each parameter, with 20 samples each. The main panel is color-coded by the root-mean-square (RMS) of model residuals. The bottom panel shows the RMS values with respect to μ for with each value of η (gray lines); the RMS values averaged across all η are shown in black. The right panel is the same as the bottom, but for η. The blue dot in each panel indicates the preferred model with $\mu = 0.7$ and $\eta = 1.4$.

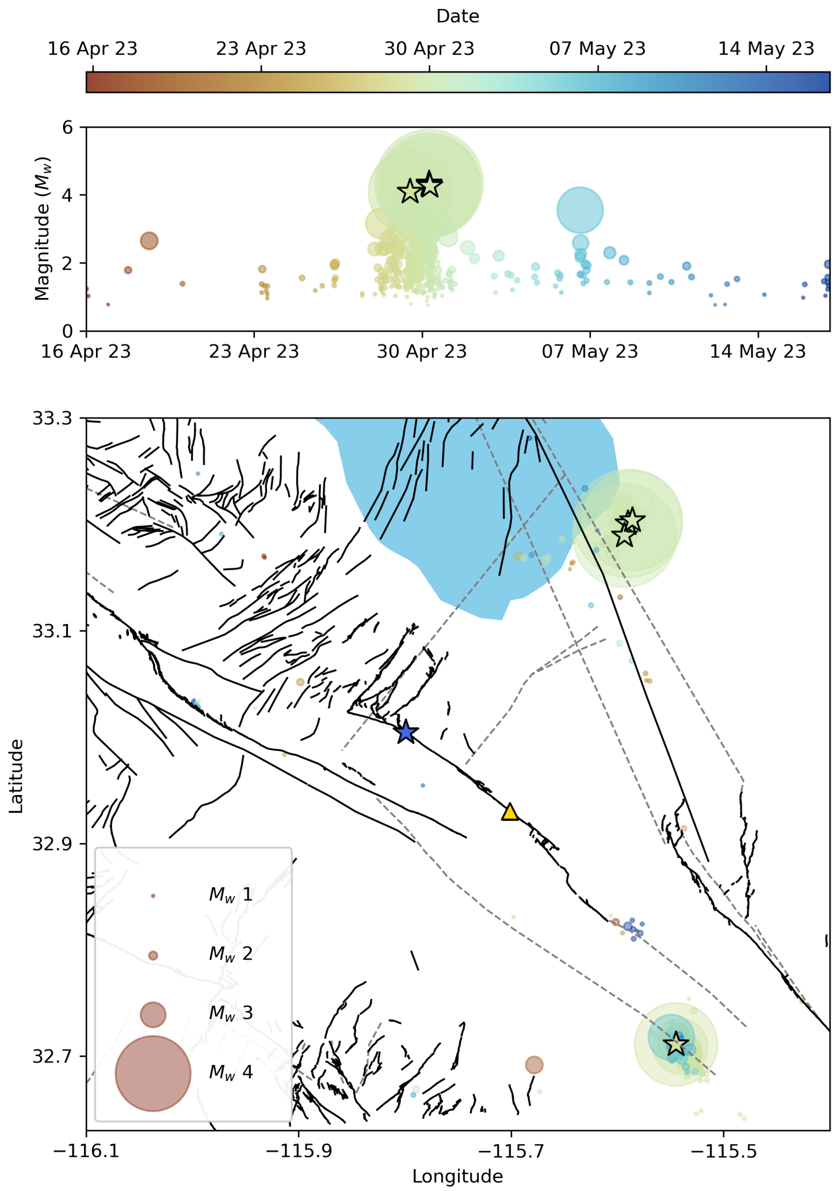

Figure S7. Local seismicity one month prior to slip being detected by the COL creepmeter (16 April 2023 - 16 May 2023). Quaternary faults are shown as black lines (USGS, 2020), while blind faults from the Southern California Earthquake Center Community Fault Model are shown as dashed gray lines (Shaw et al., 2015). The yellow triangle shows the location of creepmeters installed near Imler Road. The blue star indicates the nucleation site of initial slip on the SHF which initiated some time between 3-15 May 2023. The hypocenters of four M_w 4+ events occurring between 29-30 April 2023 are shown as light green stars.

References

Allen, C. R., Wyss, M., Brune, J. N., Grantz, A., & Wallace, R. E. (1972). *Displacements on the Imperial, Superstition Hills, and San Andreas Faults Triggered by teh Borrego Mountain Earthuake.* (Tech. Rep.).

Aster, R. C., Borchers, B., & Thurber, C. H. (2018). *Parameter estimation and inverse problems.* Elsevier.

Bilham, R., & Castillo, B. (2020). The July 2019 Ridgecrest, California, Earthquake Sequence Recorded by Creepmeters: Negligible Epicentral Afterslip and Prolonged Triggered Slip at Teleseismic Distances. *Seismological Research Letters*, *91*(2A), 707–720.

Brodsky, E. E. (2003). A mechanism for sustained groundwater pressure changes induced by distant earthquakes. *Journal of Geophysical Research*, *108*(B8), 2390.

Jonsson, S. (2002). Fault Slip Distribution of the 1999 Mw 7.1 Hector Mine, California, Earthquake, Estimated from Satellite Radar and GPS Measurements. *Bulletin of the Seismological Society of America*, *92*(4), 1377–1389.

Klimeš, J., Rowberry, M. D., Blahůt, J., Briestenský, M., Hartvich, F., Košťák, B., Rybář, J., Stemberk, J., & Štěpančíková, P. (2012). The monitoring of slow-moving landslides and assessment of stabilisation measures using an optical–mechanical crack gauge. *Landslides*, *9*(3), 407–415.

Kohler, W. M., & Fuis, G. S. (1986). Travel-time, time-term, and basement depth maps for the Imperial Valley region, California, from explosions. *Bulletin of the Seismological Society of America*, *76*(5), 1289–1303.

Kostak, B., & Popp, K. (1966). Moiré strain gauges. *Strain*, *2*(2), 5–16.

Košťák, B. (1969). A new device for in-situ movement detection and measurement. *Experimental Mechanics*, *9*(8), 374–379.

Martí, X., Rowberry, M. D., & Blahůt, J. (2013). A MATLAB® code for counting the moiré interference fringes recorded by the optical-mechanical crack gauge TM-71. *Computers & Geosciences*, *52*, 164–167.

Nikkhoo, M., & Walter, T. R. (2015). Triangular dislocation: an analytical, artefact-free solution. *Geophysical Journal International*, *201*(2), 1119–1141.

Rymer, M. J., Boatwright, J., Seekins, L. C., Yule, D., & Liu, J. (2002). Triggered Surface Slips in the Salton Trough Associated with the 1999 Hector Mine, California, Earthquake. *Bulletin of the Seismological Society of America*, *92*(4), 1300–1317.

Sharp, R. V., Rymer, M. J., & Lienkaemper, J. J. (1986). Surface displacement on the Imperial and Superstition Hills faults triggered by the Westmorland, California, earthquake of 26 April 1981. *Bulletin of the Seismological Society of America*, *76*(4), 949–965.

Shaw, J. H., Plesch, A., Tape, C., Suess, M. P., Jordan, T. H., Ely, G., Hauksson, E., Tromp, J., Tanimoto, T., Graves, R., Olsen, K., Nicholson, C., Maechling, P. J., Rivero, C., Lovely, P., Brankman, C. M., & Munster, J. (2015). Unified Structural Representation of the southern California crust and upper mantle. *Earth and Planetary Science Letters*, *415*, 1–15.

Simons, M. (2002). Coseismic Deformation from the 1999 Mw 7.1 Hector Mine, California, Earthquake as Inferred from InSAR and GPS Observations. *Bulletin of the Seismological Society of America*, *92*(4), 1390–1402.

Tymofyeyeva, E., Fialko, Y., Jiang, J., Xu, X., Sandwell, D., Bilham, R., Rockwell, T. K., Blanton, C., Burkett, F., Gontz, A., & Moafipoor, S. (2019). Slow Slip Event On the Southern San Andreas Fault Triggered by the 2017 Mw 8.2 Chiapas (Mexico) Earthquake. *Journal of Geophysical Research: Solid Earth*, *124*(9), 9956–9975.

USGS. (2020). *Quaternary Fault and Fold Database for the Nation.*

Wang, K., & Fialko, Y. (2018). Observations and modeling of co- and postseismic deformation due to the 2015 M_w 7.8 Gorkha (Nepal) earthquake. *J. Geophys. Res.*, *123*(1), 761–779.

Wei, M., Sandwell, D., & Fialko, Y. (2009). A silent M_w 4.7 slip event of October 2006 on the Superstition Hills fault, southern California. *Journal of Geophysical Research*, *114*(B7), B07402.

Wei, M., Sandwell, D., Fialko, Y., & Bilham, R. (2011). Slip on faults in the Imperial Valley triggered by the 4 April 2010 Mw 7.2 El Mayor-Cucapah earthquake revealed by InSAR. *Geophysical Research Letters*, *38*(1).